ADVANCED FUNCTIONAL MATERIALS
www.afm-journal.de

Biologically-Inspired Melt Electrowriting for the Generation of Highly Biomimetic Functional Myocardium

*Olalla Iglesias-García, María Flandes-Iparraguirre, Pilar Montero-Calle, Ricardo M. Rosales, Asier Ullate-Agote, Andrea Sánchez-Bueno, Eduardo Larequi, Ilazki Anaut-Lusar, Nicolás Laita, Aida Oliván-Viguera, Elena Iglesias, Gloria Abizanda, Patxi San Martín-Úriz, Paula Aguirre-Ruiz, Xabier L. Aranguren, Manuel García de Yébenes, Juan José Gavira, Miguel Ángel Martínez, Estefanía Peña, Manuel Doblaré, Elena M. de-Juan-Pardo, Esther Pueyo, Felipe Prosper, and Manuel M. Mazo Vega**

In the heart, the specific 3D structure of myocardial layers produces an efficient ejection of blood. When myocardial infarction strikes, this architecture is disrupted, adding a disarranged contraction to the decreased availability of pumping units (cardiomyocytes, CMs). In this work, the alignment of cardiac fibers in a large animal model (pig) is characterized and employ melt electrowriting (MEW) to fabricate a bio-inspired scaffold with diamond-shaped pores. Using human-induced pluripotent stem cell-derived CMs and cardiac fibroblasts, human cardiac tissues with a biomimetic in-plane contraction are generated. MEW-diamond tissues beat macroscopically for over 1 month, with significantly faster kinetics, increased force, and higher conduction velocity than those based on square or rectangular pores. The diamond design induces a specific hiPSC-CM alignment resulting in the observed in-plane contraction. Transcriptomic analysis using bulk RNA-seq reveals diamond-MEW tissues present features of maturation as compared to traditional 2D cultures. Finally, the bio-inspired cardiac tissues are employed to treat an infarction model in athymic rats, showing a significant benefit on systolic function and remodeling, tied to the presence of large grafts of human cells remuscularizing the ventricular wall. All in all, it is demonstrated that the new design generates superior human cardiac tissues with therapeutic capacity.

1. Introduction

The human heart is a complex biological structure, where pumping efficiency is maximized through the specific geometrical arrangement of its contractile units, the cardiomyocytes (CMs), and their surrounding extracellular matrix (ECM). The specifics are still a matter of debate, with different systems proposed, such as the helical myocardial band (also termed of Torrent-Guasp), or the so-called myocardial mesh models.[1,2] Independently of these theoretical frameworks, CMs in the left ventricular (LV) wall vary their orientation throughout the thickness of the tissue.[3] This gives rise to a highly coordinated contraction-torsion movement, responsible for the adequate ejection of blood, as well as an appropriate electrical propagation. Disturbance of this exquisite arrangement can occur due to an underlying disease, but purely structural alterations can also result in organ

O. Iglesias-García, M. Flandes-Iparraguirre, P. Montero-Calle, A. Ullate-Agote, A. Sánchez-Bueno, I. Anaut-Lusar, E. Iglesias, G. Abizanda, X. L. Aranguren, M. M. Mazo Vega
Bioengineering Program
Enabling Technologies Division
Cima Universidad de Navarra, and Instituto de Investigación Sanitaria de Navarra (IdiSNA)
Pamplona 31008, Spain
E-mail: mmazoveg@unav.es

The ORCID identification number(s) for the author(s) of this article can be found under https://doi.org/10.1002/adfm.202420106

DOI: 10.1002/adfm.202420106

R. M. Rosales, N. Laita, A. Oliván-Viguera, M. Á. Martínez, E. Peña, M. Doblaré, E. Pueyo
Aragón Institute for Engineering Research (I3A)
University of Zaragoza
Zaragoza 50018, Spain

E. Larequi, G. Abizanda, F. Prosper, M. M. Mazo Vega
Hematology and Cell Therapy Area, Cancer Center Clínica Universidad de Navarra (CCUN)
Clínica Universidad de Navarra
Instituto de Investigación Sanitaria de Navarra (IdiSNA)
Pamplona 31008, Spain

P. San Martín-Úriz, P. Aguirre-Ruiz, F. Prosper
Hemato-Oncology Program
Cancer Division
CIMA Universidad de Navarra
Instituto de Investigación Sanitaria de Navarra (IdiSNA)
Pamplona 31008, Spain

malfunction. For example, myocardial infarction (MI) not only causes the death of a significant portion of cardiac cells, decreasing the pool of work-generating units, but also alters their global arrangement, thus reducing global contraction.[4,5] This natural cardiac 3D structure is a result of complex embryonic movements, and the contribution from several progenitor populations at different stages of development.[6,7] Structural remodeling continues after birth, with the rise of hemodynamic demand, and through infancy and puberty, till the completion of CM maturation around the second decade of life.[8] These natural processes can be the source of inspiration for the biofabrication of human cardiac tissue in the lab, but 20 years is too long a scale. This is especially relevant given the pressing need for the obtaining of human myocardium, as cardiovascular diseases are the number one killer worldwide, with MI being the first single cause of death,[9] and a significant source of expenditure.[10]

Opportunity is ripe. The bursting of boundaries brought about by the almost concomitant development of additive manufacturing technologies and cellular reprogramming, has provided excellent breakthroughs across different scales. The Dvir lab was one of the first to produce personalized, anatomically relevant, and scaled models of human myocardium, in the form of both patches and hearts. Omental tissue was processed into a hydrogel, whilst cells were reprogrammed into human induced pluripotent stem cells (hiPSCs), later to be differentiated into CMs and endothelial cells.[11] The Feinberg group fine-tuned a collagen-based bioink and similarly employed a support bath (freeform reversible embedding of suspended hydrogels or FRESH), to build hiPSC-cellularized small ventricles with cohesive functionality and coordinated electrical activity.[12] The team of Brenda Ogle took a slightly different approach, with a more complex biomaterial ink formulation which included gelatin methacrylate (GelMA), collagen methacrylate (ColMA), fibronectin, and laminin-III. The resulting bioink from combining this mixture with hiPSCs was printed into the shape of a mini-ventricle and cardiac differentiation induced, achieving physiological drug-responsiveness and macroscopic beating, amongst others.[13] Recently, the group of Felix Engel has developed an improved support bath and biomaterial ink (collagen-hyaluronic acid-based) formulation and applied it to the printing of cardiac constructs with increasing complexity and long-term culture capacity.[14] Other approaches have involved the biofabrication of cardiac structures including cardioids.[15] Overall, these scaffold-free methods can generate functional, physiologically-shaped constructs, but alignment is usually limited. Inclusion of polymeric cues or additional fabrication steps have demonstrated the capacity to surpass this limitation, progressing toward the recapitulation of the already structured alignment of CMs within each layer of the LV wall has seldom been explored using biofabrication technologies, as achieving programmed directionality on CMs is not trivial. Choi et al showed the 3D printing of gelatin fibers within an alginate-gelatin ink. The pre-formed fibres provided alignment cues for the CMs, that were seeded after printing, delivering a functional ventricle model with coordinated impulse propagation.[16] The Lewis group took clever advantage of the sheer produced during bioprinting to induce hiPSC-derived CM (hiPSC-CMs) alignment.[17] This method delivered high-density units, that could be programmed with a pre-designed alignment to achieve different functionalities. In general, this approach has shown better results than the inclusion of more conventional 3D-printed polymeric fibers, which generally results in stiffer constructs with diminished contractile capacity.[18] In addition, the presence of a scaffold often occupies a high volumetric fraction, precluding the generation of high-density tissues equivalent to native human myocardium, reported in the range of 10–28 million cells per mL.[19]

Within the different biofabrication technologies, melt electrowriting (MEW) is uniquely suited to surpass these limitations, tuning CM alignment and construct functionality. MEW can 3D print micrometric fibers (usually 10–20 µm in diameter), with high precision, providing a superb control over the presented cues, as well as the mechanical environment of the to-be construct.[20] MEW scaffolds present large pores, occupying a low volume within the final construct,[21] enabling the generation of the high densities needed for human cardiac tissue engineering. We and others have already demonstrated the capacity of MEW to constitute the basis for the generation of engineered human cardiac tissues.[22,23] Moreover, we have started to decipher what is the relationship between the printed MEW scaffold, the resulting hiPSC-CM arrangement, and the resulting functionality. However, orthogonal pore geometries do not adequately recapitulate the mechanical anisotropy of cardiac tissue.[24] Similarly, although the hexagonal structures used by Castilho et al.[23] better permit reversible cyclic deformations, the statement that an hexagon better represents the honeycomb structure of the myocardium[25] is not totally accurate. This honeycomb-like pattern is produced by the cross-sectional area of CMs, whereas the cells will arrange longitudinally on scaffolds regardless of the geometry of the pore.

In the present work, we go one step further and design MEW scaffolds that recapitulate the aligned, in-plane beating of LV myocardial layers. These structures, with pores in the shape of diamonds, demonstrate better functionality, structure, and gene expression than conventional orthogonal designs (square, rectangle). A transcriptomic analysis is able to pinpoint the differences of this MEW 3D system over conventional 2D cell culture, with the former presenting higher similarity to the biological counterpart. We transplant the MEW cardiac constructs in an athymic rat model of MI, where animals treated with the 3D constructs show

M. García de Yébenes, J. J. Gavira
Department of Cardiology
Clínica Universidad de Navarra
Pamplona 31008, Spain

M. Doblaré, E. Pueyo
Aragon Institute of Health Research (IIS Aragon)
Zaragoza 50009, Spain

M. Doblaré
Nanjing Tech University
Nanjing 211816, China

E. M. de-Juan-Pardo
School of Engineering & T3mPLATE
Harry Perkins Institute of Medical Research
QEII Medical Centre and the UWA Centre for Medical Research
The University of Western Australia
Perth WA6009, Australia

F. Prosper
Centro de Investigación Biomédica en Red de Cáncer (CIBERONC)
CB16/12/00489, Madrid 28029, Spain

better cardiac function, with large grafts of human cells surviving for the duration of the in vivo study (4 weeks). Finally, we employ in silico simulations to investigate the proarrhythmic potential of our designs when interfaced with porcine and human myocardium.

2. Results and Discussion

2.1. Using MEW to Generate Scaffolds with Potential to Generate Aligned Contraction

Current models determine that CMs within the ventricular wall are aligned, and that the direction of this alignment varies throughout the thickness to deliver a healthy contraction-torsion motion.[26] To assess the degree of this change and determine if this can be mimicked using MEW, we performed a directional analysis on Hematoxylin-Eosin -stained pig myocardial histological preparations, sampled throughout the thickness of the LV free wall (**Figure 1A**), at the location corresponding to the area of MI in this experimental model.[27] Using the Orientation J feature of ImageJ, the analysis (N = 6 porcine hearts Figure 1B) showed that CM alignment varied 48.56 ± 5.95° from epicardium to endocardium, equating to a change of 5.94 ± 1.38°/mm (Figure 1C), which is similar to what Walker and co-workers reported for the sheep heart.[28] This magnitude of change can be adequately reproduced using MEW. Within the possible geometries available for printing with MEW, orthogonal pores had been already explored by us and others,[22,29] but they were mostly isometric, whereas cardiac tissue is characterized by the said strong anisotropy, leading to efficient unidirectional contraction within one myocardial layer. Hexagons, a more advanced geometry, are also similarly limited in this regard.[23] Therefore, we designed a novel scaffold with pores in the shape of diamonds. Diamonds feature a prominent direction of lesser resistance along the minor diagonal, and would potentially constitute a good fit for our hypothesis: that the mechanical environment and alignment cues provided by the fibrillary MEW scaffold can optimize macroscopic function of biofabricated human myocardium toward a unidirectional, in-plane contraction. We designed a G-code for the printing of 2 × 1 mm (large x small diagonal) pores (Supporting information), as MEW scaffolds based on medical grade poly-ϵ-caprolactone (mPCL) are substantially rigid if designed with small pores,[22] which would limit the overall construct macroscopic contraction. With a therapeutic perspective in mind, the more rigid the MEW scaffold, the more work-seeded CMs would have to invest in contracting this structure, which would then diminish the amount available for transmission to any underlying diseased myocardium. It is plausible that a careful gauging of the relation between pore-dimensions and resulting functionality could render a more optimized set of dimensions, though that lies outside the scope of this work. In order to ensure a precise and homogeneous scaffold deposition, and to minimize fiber diameter (also impacting scaffold rigidity), MEW conditions were optimized, namely feed pressure, voltage, collector distance, and collector speed. Figure 1D depicts the effect of the different variables on the fiber thickness. As shown, for a constant collector distance of 8 mm, an increase in the feed pressure translates into thicker fibers. Conversely, augmenting either the voltage or the collector speed results in diminished fiber diameters. Hence, the thickest fibers were obtained at the combination of highest pressure and lowest voltage and speed, measuring 64.88 ± 0.35 µm for 3 bars, 4.5 kV, and 200 mm min^{-1}. On the other hand, the thinnest fibers, of 9.44 ± 0.39 µm in diameter, were achieved with the experimental combination of lowest pressure (1 bar) and highest voltage (6.5 kV) and speed (800 mm min^{-1}) of the examined values (Figure 1Di). However, homogeneous and continuous printing of full scaffolds at this low end of achievable thickness was challenging, especially impacting fiber deposition patterns. Here, the most important factor for fiber deposition accuracy is the relationship between the polymer mass flow at the nozzle and at its contact point in the collector plate. In practice, this can be assimilated to the relationship between the jet and collector velocities, V_{jet} and V_{plate}. Ideally, optimal fiber collection happens if $V_{plate} = V_{jet}$; this velocity is known as critical translation speed (CTS) and is specific of each set of conditions, including external variables such as ambient temperature. When the collector plate speed is not fast enough to accommodate the amount of polymer being deposited ($V_{plate} < V_{jet}$), coiling occurs, and fiber piles up as a result.[30,31] The slower the plate, the bigger the degree of fiber coiling, as can be seen in Figure 1Dii. On the other hand, when $V_{plate} > V_{jet}$, the polymer jet does not have enough time to be completely deposited, as the plate "pulls" from it. This results in an increased fiber lag, which is the distance between the projection of the nozzle on the collector plate and the spot in which the fiber actually contacts the plate. In turn, the longer lag translates into a poorer accuracy deposition, especially the regions where the path involves a sharp change in direction, such as the edges of the scaffold (Figure 1Diii). The consistent testing and set up of these parameters resulted in the following final conditions: 2 bars, 6.5 kV, and 800 mm min^{-1}, with a head-to-collector distance of 8 mm. In this manner, large scaffolds with the designed pores in the shape of diamonds could be reproducibly printed (Figure 1E). Scanning electron microscopy (SEM) imaging (Figure S1, Supporting Information) shows a precise stacking of fibers and layer bonding.

2.2. Diamond-Pore MEW Design Produces Human Constructs with Aligned Macroscopic Contraction

In order to test the capacity of the diamond-pore MEW scaffolds to produce the hypothesized contraction, we differentiated CMs and cardiac fibroblasts (CFs) from hiPSCs. Both phenotypes were derived using chemically-defined protocols,[32,33] yielding high-purity cultures as determined by FACS (Figure S2, Supporting Information for an extended cellular characterization). Cells were differentiated in separate substrates, detached, mixed in in a 9:1 proportion (hiPSC-CMs: hiPSC-CFs), embedded in a fibrinogen precursor and casted on oxygen-plasma treated MEW scaffolds (**Figure 2A**). This 9:1 proportion was chosen to boost contractility of the constructs by maximizing hiPSC-CM content whilst retaining a proportion of stromal cells, as previously used by others.[34–37] 10-layer scaffolds were printed, in order to avoid potential issues with nutrient and oxygen diffusion, since these would result in a thickness below the 200 µm limit,[38] as each fiber has a thickness of ≈17 µm. Fibrinogen was crosslinked to fibrin upon the addition of thrombin, through a 60-min incubation at 37 °C, after which samples were cultured for 2 weeks.

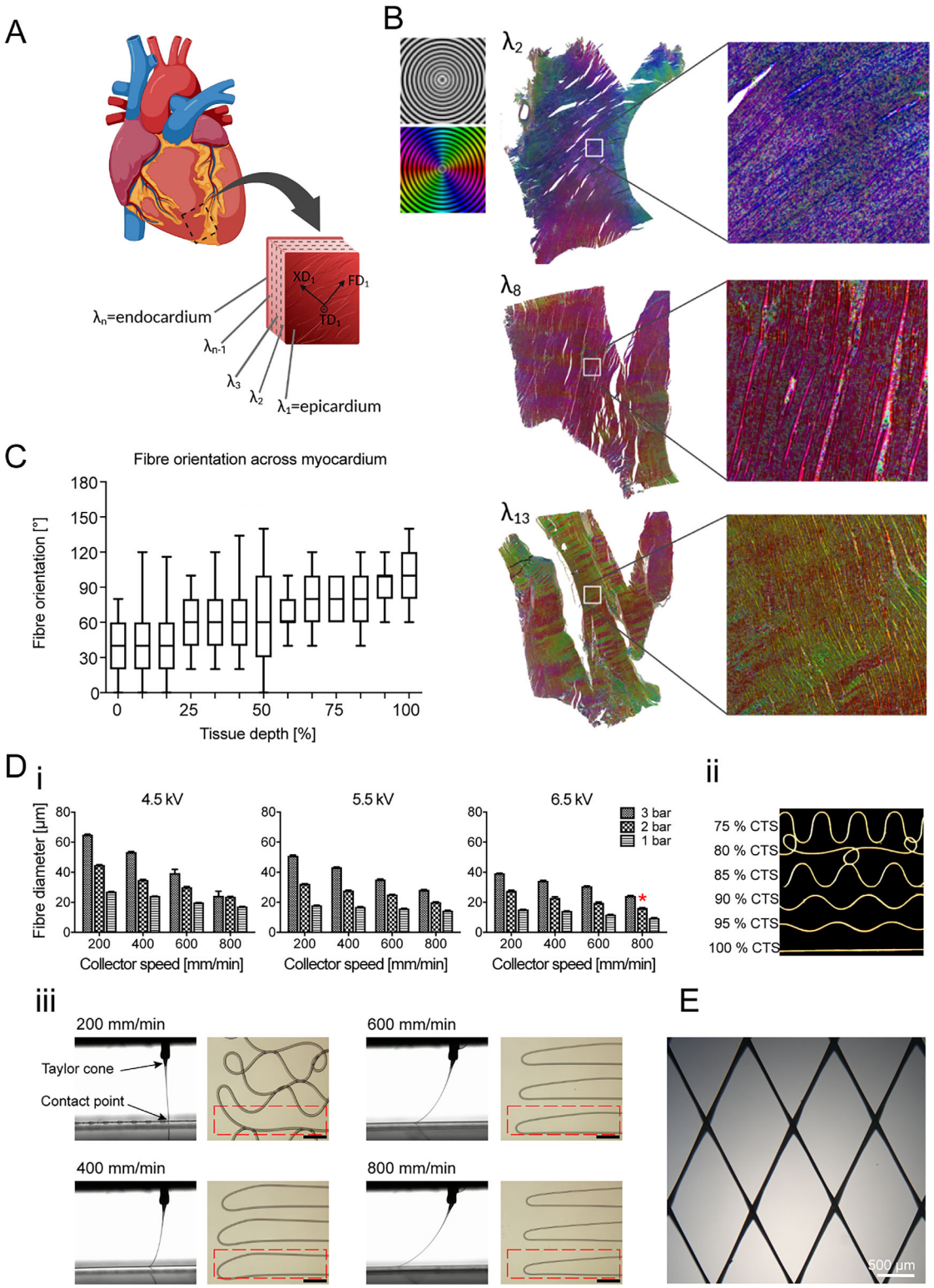

Figure 1. Biomimetic MEW scaffold design and fabrication. A) Schematics of alignment variation throughout the thickness of the myocardial wall and area of sampling. B) Alignment analysis (color-coded) and representative porcine heart tissue processed for H&E staining and orientation assessed, with $\lambda = 1$ being the layer closer to epicardium. C) Quantitative assessment of alignment (N = 6 hearts, 20–30 slides per heart, data shown as median (Q1,Q3)). D) MEW printing optimization. i) Effect of varying voltage and pressure on fiber dimensions, (ii) dealing with coiling by achieving right CTS and (iii) collector speed. E) Image of full scaffold printed under final conditions: 6.5 kV, 800 mm min^{-1} 2 bar.

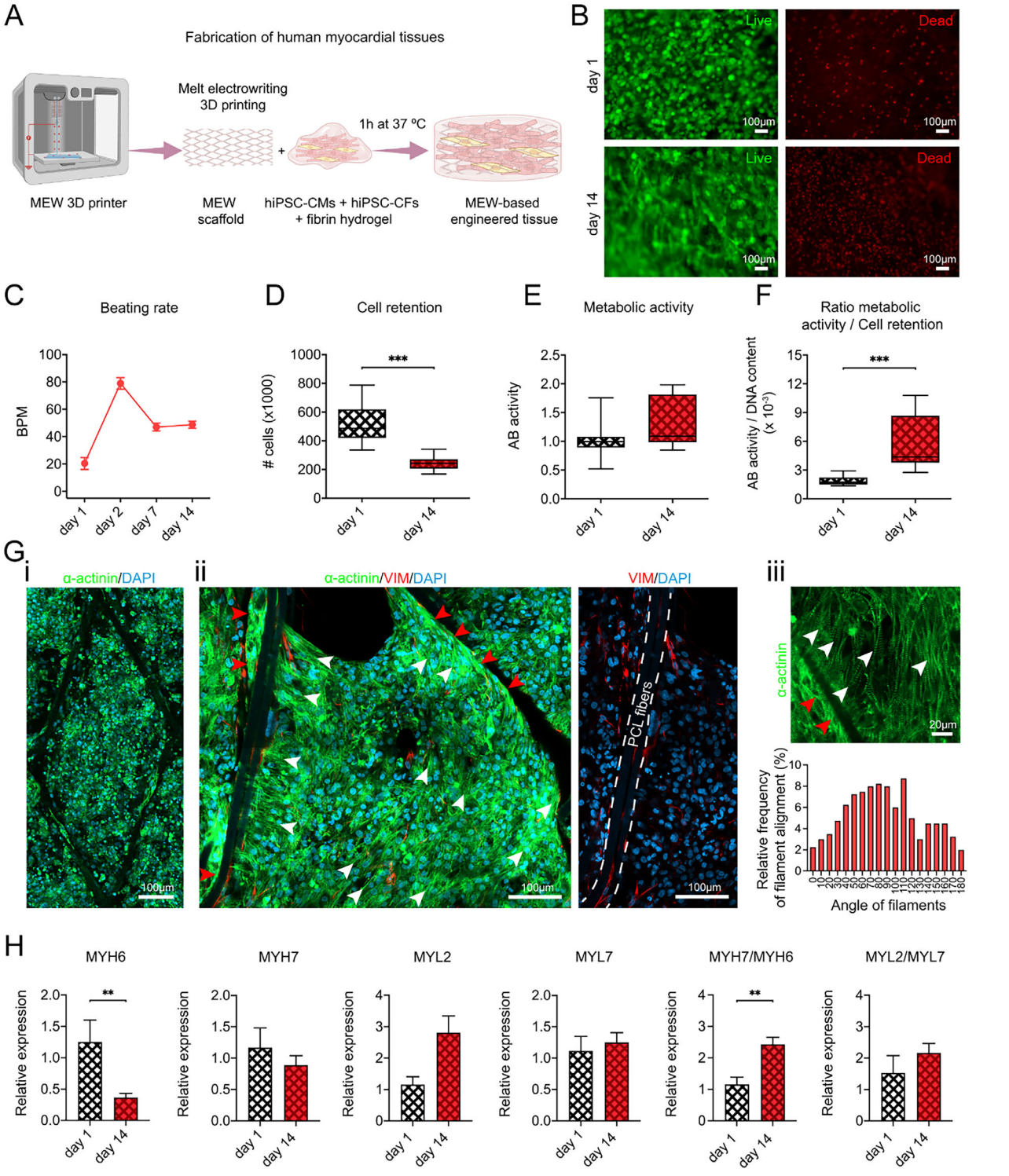

Figure 2. Diamond-pore MEW scaffolds generate in-plane contracting tissues. A) Scheme of MEW-based engineered tissue fabrication (made with BioRender.com). B) Live/dead staining on days 1 and 14, showing overall cellular morphology, as well as presence of dead cells. C) Evolution of macroscopic beating rate during culture. D) Quantitation of cell retention via PicoGreen assay, showing a decrease in the number of cells. E) Overall stability of metabolic activity, measured by AlamarBlue (AB), resulting in (F) a significant increase in the ratio of metabolic activity/cell number. G) Confocal immunofluorescent (IF) analysis of cell location within the structure of the tissues, demonstrating (i) complete filling of the 3D space, with hiPSC-derived cells (ii, left panel) following the fiber direction (red arrowheads) or arranging perpendicular to it (white arrowheads) when in its proximity, whilst adopting a more random orientation within the pore, (ii, right panel) with hiPSC-CFs interspersed; (iii) quantification of overall sarcomeric alignment. H) Gene expression analysis by RT-qPCR, relative to day 1 samples. Data shown as: D–F): median (Q1,Q3); C,H): mean ± SEM. N = 3–5 independent experiments, n = 2–4. E): paired t-test; D,F,H): independent t-test; $^{**}p < 0.01$; $^{***}p < 0.001$.

Live/dead staining on day 1 showed overall rounded morphology, which evolved to a more elongated one by day 14 (Figure 2B). This change in cellular morphology correlated with a distinct beating behavior, as engineered cardiac tissues showed localized contraction already 1 day after generation, with rhythm peaking on day 2 ≈80 beats per minute (bpm), and decreasing thereof and becoming stable ≈60 bpm (1 Hz) by day 14 (Figure 2C). A significant proportion of cell death was evident, with roughly half of the viable cells lost in the 2-week culture period (Figure 2D). Significantly, the metabolic activity was maintained (Figure 2E), meaning that although cells were lost, the ones that remained were significantly more active (ratio metabolic activity to DNA, Figure 2F), pointing toward a potential increase in their maturity.

Tissues showed macroscopic contraction, evident to the naked eye, which was aligned on the lesser diagonal of the diamonds (Video S1, Supporting Information). This contraction reached a magnitude big enough to produce motion (Video S2, Supporting Information). Cells in constructs were evenly distributed, generating thickly populated tissues, in contrast to what has previously been shown by Castilho et al,[23] where the use of collagen type I as the embedding hydrogel led to a retraction of the cellularised areas toward the fibers, probably due to the mechanical behavior of collagen itself. Here, hiPSC-derived cells fully filled the pores (Figure 2Gi) and attached to fibers, with α-actinin$^+$ hiPSC-CMs displaying well-arranged sarcomeres and VIM$^+$ hiPSC-CFs distributed throughout the tissue (Figure 2Gii). As shown by our group in the past,[22] cells were able to interact and follow the MEW fibers, whilst others arranged themselves more perpendicular to them (Figure 2Gii, red and white arrowheads, respectively), and those deep into the pore were more randomly distributed. Quantification of the sarcomeric alignment resulted in a distribution of ≈51% in the range of 70 ± 30 ° (referred to the direction of the major diagonal of the diamond, Figure 2Giii), which coincides with the direction of contraction. Finally, the 14 days of in vitro culture did not significantly alter cellular proportions, as 8.95 ± 0.62% (mean ± SEM) of cells showed a positive staining for VIM, labeling them as CFs. Curiously, hiPSC-CFs showed a skewed geographical distribution, with significantly more cells presence in the middle of the pore as compared to the fiber and its immediate vicinity (27.77 ± 2.01% vs 72.23 ± 2.02%, $p < 0.001$ *t*-test, Figure S3, Supporting Information).

Gene expression analysis of myosin isoforms by RT-qPCR showed a downregulation of the expression of the immature form of myosin heavy chain, *MYH6*, whilst the expression of the mature *MYH7* remained unchanged, leading to a significant increase in the ratio *MYH7/MYH6*. The light chain isoforms related to atrial (*MYL7*) and ventricular (*MYL2*) phenotypes, or their ratio (*MYL2/MYL7*) also remained unchanged during the 2-week period (Figure 2H). As a whole, these results demonstrate that diamond-pore MEW scaffolds can sustain the formation of human cardiac-engineered tissues using hiPSC-derived cells (CMs and CFs), and that they undergo an evident maturation during 2 weeks. Importantly, the initial hypothesis of the diamond-pore design being able to deliver aligned, unidirectional contractile tissues is confirmed.

2.3. Diamond-MEW Human Cardiac Engineered Tissues Display Features of Maturation at Transcriptomic Level

To analyze in depth the influence of the mechanical environment on the evolution, maturation, and biomimetism of the human biofabricated tissues, we studied their transcriptomic profile by bulk RNA-seq. Cells at a 9:1 hiPSC-CMs: hiPSC-CFs ratio were either embedded in the fibrin hydrogel in combination with the diamond-MEW designs or seeded on standard 2D culture plates at the same density, maintained for up to 30 days and characterized at the transcriptomic level (**Figure 3A**). A principal component analysis (PCA) showed a clear separation of the 3D samples from the 2D cultures in the first component, pointing to an impact of the mechanical environment in the different cell culture conditions (Figure 3B). A differential expression analysis between 3D and 2D conditions at day 30 showed significant upregulation of genes related to cardiac maturity, lipid metabolism and potassium metabolism in the 3D tissues compared to cells cultured in 2D (Figure 3C). In contrast, we detected a significantly higher expression of ECM related genes in 2D cultures highlighting, in agreement with previous studies, the limitations of 2D cultures with respect to the in vivo reality.[39] Additionally, several genes involved in the regulation of cellular stress and hypoxia response were detected in 3D, which can either reflect the decrease in cell viability observed in cultured 3D tissues or suggest a limited oxygen diffusion within the 3D environment, in spite of the chosen thickness (below the 200 µm limit). This is critical for engineered cardiac tissues due to the high metabolic demand of CMs, which require a controlled microenvironment with adequate supply of oxygen and nutrients.[40] Notably, the most relevant biological differences between 3D and 2D were associated with an upregulation in processes related to cardiac contraction and a down-regulation in processes related to ECM organization (Figure 3D; Figure S4, Supporting Information). Clustering differentially expressed genes (DEG) into expression patterns revealed that most genes behave similarly in 2D even after being cultured for 30 days, indicating that 2D conditions do not provide the physiological relevant cues to favor cardiac differentiation and maturation. On the other hand, in 3D conditions their expression differ, presenting an upregulation for processes related to heart contraction and downregulation of ECM related processes (Group 1 and 3 respectively in Figure S4, Supporting Information). These results demonstrate that the diamond-MEW-based design provides a highly biomimetic and more realistic environment to actively drive cardiac tissue maturation, presenting a higher similarity to their cardiac counterpart. It would be highly interesting to pursue additional methods to further the maturation of these constructs. Ramped-up electrical stimulation has provided on of the most advanced examples of maturation, with tissues displaying a positive force-frequency relationship, increased contractility, and adult-like ultrastructure.[41]

2.4. Mechanical Characterization of MEW Scaffolds

To comprehensively characterize the mechanical response of the scaffolds, both uniaxial and biaxial testing are needed

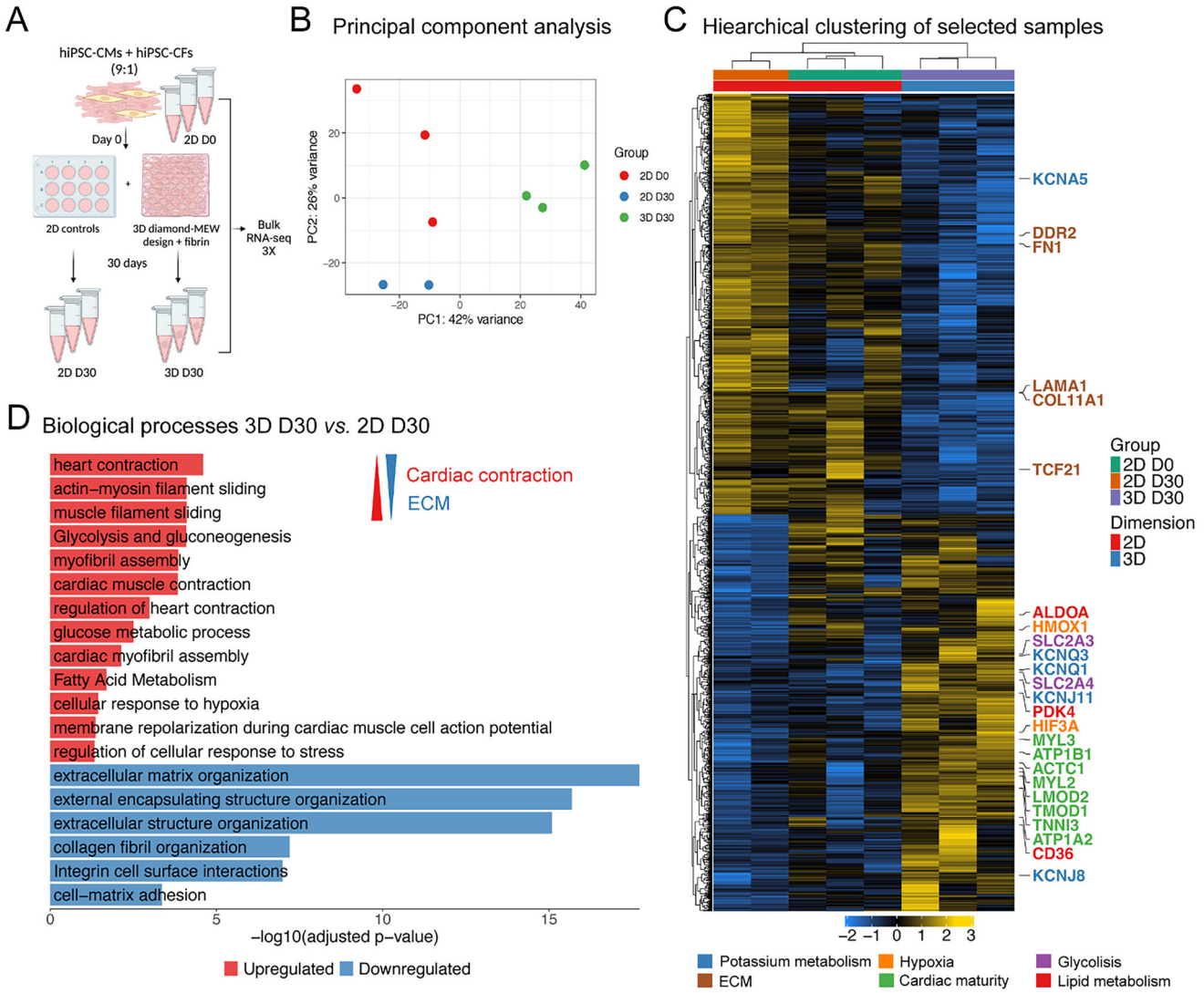

Figure 3. RNA-seq analysis of diamond-MEW cardiac minitissues. A) A schematic diagram of the cell culture condition, tissue fabrication, and sample processing for RNA-seq analysis (made with BioRender). 2D cultures prior to tissue generation (day 0): 2D D0; 2D cultures at day 30: 2D D30); 3D tissues at day 30: 3D D30). B) Principal component analysis (PCA) for 3D (N = 3) and 2D culture conditions (N = 3 (day 0), N = 2 (day 30)). C) Heatmap showing scaled expression for DEGs (adjusted *p*-value < 0.05 and absolute log2FC > 1) between 3D and 2D culture conditions at day 30. Certain genes are colored according to their biological function. D) Bar plot showing selected gene sets from a gene ene over-representation analysis using the Gene Ontology (GO) biological processes, BioPlanet, and MSigDB Hallmarks databases, considering the DEGs up- and down-regulated in 3D tissues compared to 2D cultures at day 30.

(**Figure** 4A). The structural anisotropy plays a crucial role in influencing the alignment of cell contraction, particularly as cardiac cells tend to exert contractile forces along the less mechanically demanding direction of their surrounding medium.[42] Therefore, assessing the anisotropy under uniaxial loading conditions provides insights into the alignment of cell contraction in each design. Additionally, given that the scaffold will experience biaxial loading during ventricular expansion, biaxial characterization is crucial to understand its impact on cardiac tissue post-implantation.

As anticipated, the square geometry exhibits complete isotropic behavior in both biaxial and transversal uniaxial tests (Figure 4B). The rectangular geometry demonstrates some degree of anisotropy in both testing conditions but maintains high stiffness in both directions, even at low strain levels, similar to the SQ geometry. In contrast, the diamond geometry exhibits the highest degree of anisotropy, displaying virtually zero stiffness in its shortest direction, even beyond a 50% deformation. This suggests that the diamond geometry is likely to promote contraction more effectively in this shorter direction compared to the other designs. Biaxial tests (Figure 4C) reveal a consistent behavior with uniaxial tests. Once again, the diamond scaffolds exhibit the lowest isotropy ratio, followed by the rectangular geometry and the SQ geometry. This is further detailed in **Table** 1. It is noteworthy that the diamond geometry shows early failure in its longest direction during uniaxial conditions when compared to

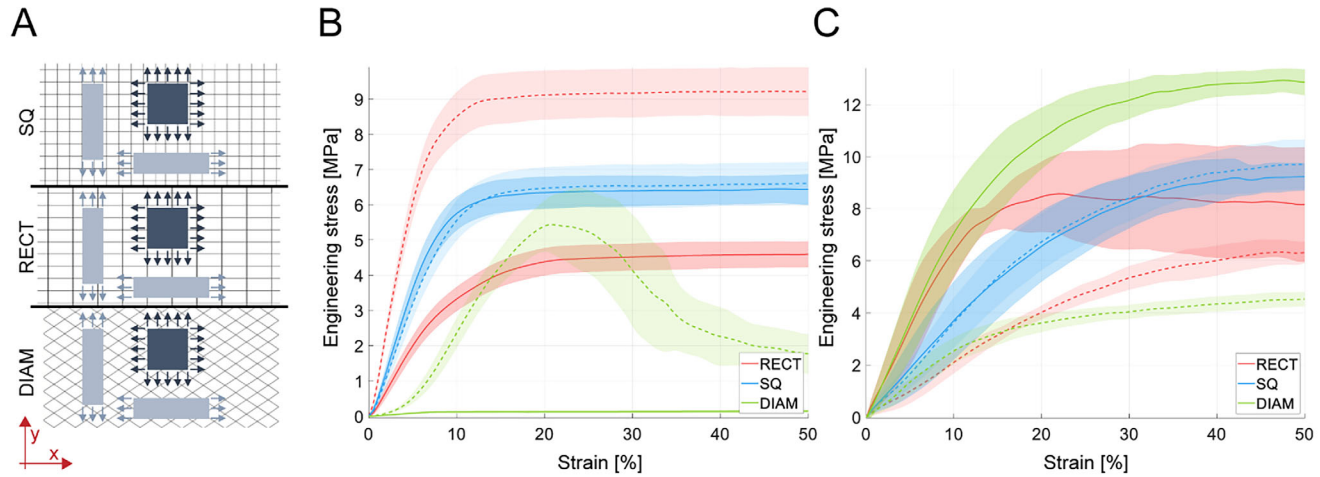

Figure 4. Experimental results for mechanical tests (made with BioRender). A) Overview of sample preparation for uniaxial (blue) and biaxial (pink) assays. B) Mean uniaxial test results. C) Equibiaxial (right) results for the three compared geometries. Dotted lines represent the longest direction of each geometry (x-axis) and solid lines the shortest one (y-axis). SQ: square; RECT: rectangular; DIAM: diamond.

the other geometries, indicating a potentially plastic behavior in that direction. However, this issue is not observed in biaxial tests. Given that the scaffolds will operate under biaxial conditions after implantation, this specific uniaxial failure is not considered a concern. Consequently, the diamond pattern appears to offer significant advantages over the other designs. It displays a considerably more anisotropic response (≈20 times more than rectangular and 40 times more than square), substantially improving the alignment of embedded cells. Furthermore, its biaxial response remains adequate for the analyzed deformation level (50%), surpassing physiological condition expectations.

2.5. Engineered Tissues Based on Diamond-MEW Scaffold Show Enhanced Functionality

In order to determine if the in-plane actuation delivered by the new diamond MEW designs resulted in a superior contractility, we printed scaffolds to function as cantilevers. This experiment was showcased by the Parker lab almost a decade ago,[43] and consists on a rectangular construct with only one freely contracting end. We printed cantilevers of 8 × 5 mm with MEW scaffolds with pores in the shape of squares, rectangles, and diamonds, all depicting the same pore area (1 cm^2, **Figure 5A**). In these, the short sides of rectangles and the smaller diagonal in diamonds followed the longer side of cantilevers (Figure 5B). These were seeded with 3 × 10^6 hiPSC-CMs and -CFs in a 9:1 proportion within a fibrin hydrogel, and cultured for 30 days (Figure 5B). Beating rate did not differ between the different groups, being as before stable ≈1 Hz (Figure 5C). Z-band distance measured on α-actinin-stained samples and imaged by confocal microscopy on day 30 did not show significant differences (2.00 ± 0.021, 1.96 ± 0.017, and 2.00 ± 0.016 µm, mean ± SEM for the square, rectangular and diamond-pore constructs, respectively, $p > 0.05$, Figure 5D). This roughly shows that the contractile apparatus was similarly arranged between the different architectures. In spite of being superior to reported values for Z-band spacing of hiPSC-CMs cultured on conventional plastic surfaces (≈1.6 µm)[44] and similar to electrically-stimulated advanced examples,[41] although it does not fully reach the 2.2 µm value of adult human CMs.[45] We recorded videos of the cantilevers to analyze their beating behavior in depth, as differences in magnitude were evident to the naked eye (Videos S3–S5, Supporting Information for tissues with square, rectangular, and diamond pores, respectively). Videos were processed using a point-tracking algorithm developed in MATLAB (Figure 5E). As shown in Figure 5F, when comparing the contraction length (i.e., the displacement of the tracked points between their origin at the relaxed state and their position in the contracted configuration), cardiac minitissues made with the diamond-patterned scaffolds showed a 3–4 times higher magnitude of contraction (107.10 ± 1.82 µm of displacement, versus 30.90 ± 0.20 and 24.29 ± 0.19 µm for square and rectangular pored scaffolds, respectively; p<0.001). Similarly, the contraction speed (defined here as how fast the points move from their origin to their contracted position) was 4–5-fold higher for the diamond-pored group (23.65 ± 0.24 µm s^{-1} for the diamond-patterned group, 6.83 ± 0.03 µm s^{-1} for the square-patterned and 5.12 ± 0.03 µm s^{-1} for the rectangular pattern; $p < 0.001$, Figure 5G). The direction of displacement of the tracked points with respect to the horizontal (0°) was also registered, and its quantification can be seen in Figure 5H. Results show how the diamond patterned constructs predominantly contract in the vertical direction (90°, 17.53%), with more than 50% of the tracked points aligned between 80 and 100°, and almost 75% between 70 and 110°. This direction corresponds to the short axis of the diamonds, and the direction of lesser mechanical resistance. On the other hand, both the square and rectangular pore geometries resulted in wider frequency distributions, with slightly higher peaks at 150° (16.58%) and 170° (17.19%), respectively. Finally,

Table 1. Isotropy ratios for each geometry at both loading conditions.

	RECT	SQ	DIAM
Uniaxial loading	0.485	0.980	0.024
Biaxial loading	0.470	0.974	0.302

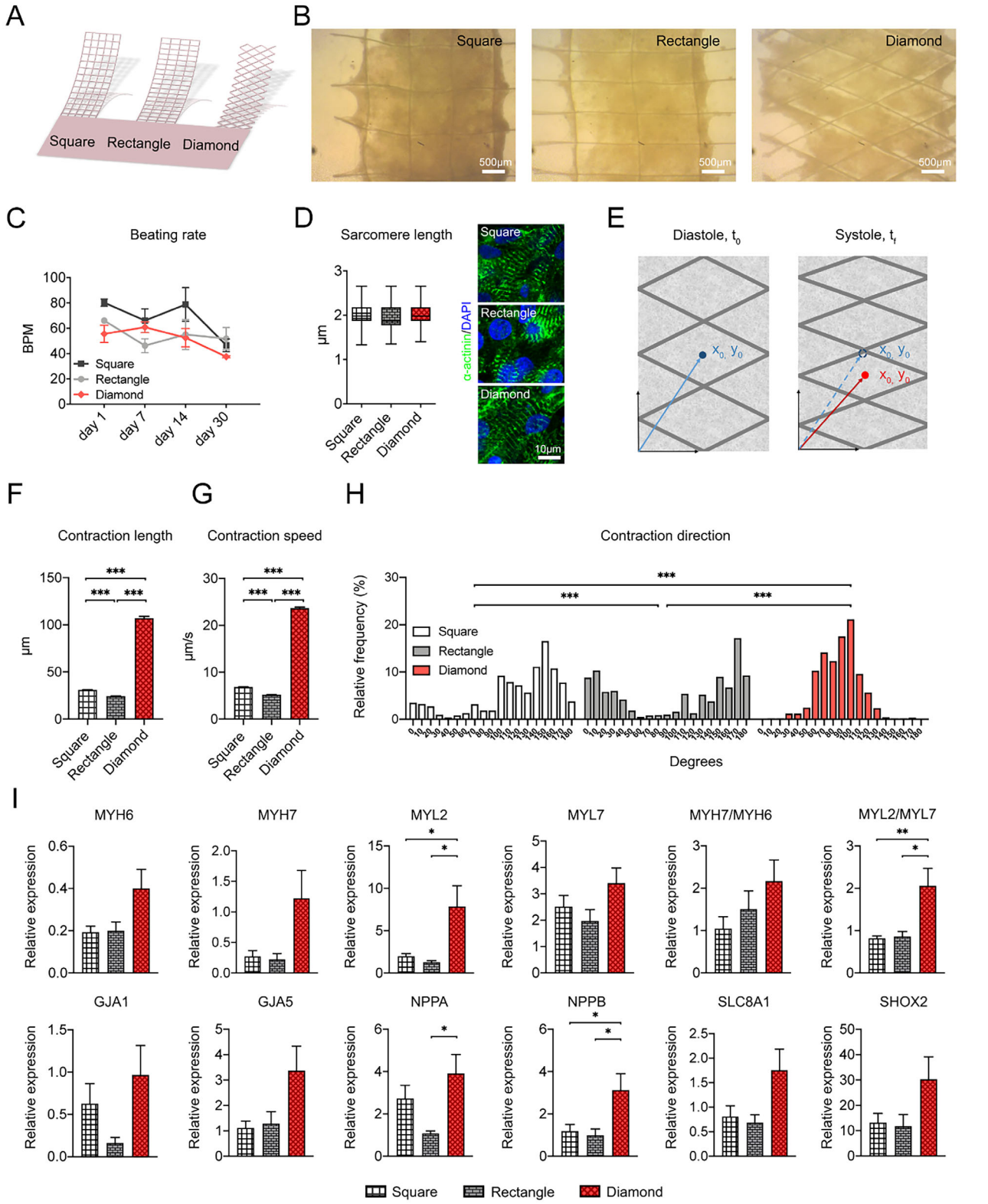

Figure 5. Comparative analysis of MEW architecture and its impact on contraction. A) Schematic representation of the cantilever experiment (made with Creo Parametric). B) Representative images of the cantilevers fabricated with the three geometries. C) The engineered myocardium showed comparable beating rate, (D) as well as similar Z-band spacing. E) Sketch of the point-tracking analysis. Diamond-pore tissues showed significantly greater (F), faster (G), and more aligned (H) contractions. I) Comparative gene expression analysis between square, rectangle, and diamond-pore MEW scaffolds. Data are shown as: C,F,G,I): mean ± SEM; D: median (Q1,Q3). ANOVA followed by HSD Tukey, $*p < 0.05$; $**p < 0.01$; $***p < 0.0001$. N = 3 independent experiments, n = 3-4.

we compared the profile of gene expression for cardiac genes on the three geometries by RT-qPCR (Figure 5I), showing the diamond designs elicited a higher expression of *MYL2* (almost four-fold), resulting also in a significantly increased *MYL2/MYL7* ratio, pointing toward a more ventricular-like phenotype. *MYH7* showed a trend toward increased expression in the diamond geometry, as well as the maturity ratio *MYH7/MYH6*, but these did not reach statistical significance. Interestingly, the genes encoding for the atrial and brain natriuretic peptides, *NPPA* and *NPPB*, were significantly increased in diamonds over the other orthogonal designs. This could have several interpretations, as *NPPA* and *NPPB* expression is high during working myocardial development, with both genes expressed in embryonic CMs (reviewed in).[46] On the other hand, *NPPA* and *NPPB* are upregulated postnatally in situations of stress or disease.[47] Although this last possibility cannot be excluded, given that even the more advanced maturation status achieved in vitro for hiPSC-CMs still equated to early-to-mid-stages of human embryonic development,[41] we expect our engineered myocardium to still display characteristics of fetal tissue, thus compatible with the former interpretation. Nevertheless, further experiments will be needed to clarify this point.

The above information can be brought together with results from the mechanical analysis to hypothesize a potential mechanism for the observed functional improvement. 3D tissues have consistently shown their capacity to improve the functionality and maturity of hiPSC-CMs,[41,48] as also shown for MEW-based tissues by us and others.[22,23] At the same time, the near zero stiffness of the diamond scaffolds on the direction of the minor diagonal (under uniaxial loading) for the deformation experienced during hiPSC-CM contraction, means a lesser proportion of the force generated by cells is employed on moving the scaffold itself, leading to a greater and faster contraction. A higher gene expression of prominent ventricular contractility-related genes such as MYL2, also supports the observed effect. However, determining whether the original source of the improvement is the 3D environment or the mechanical properties cannot be discerned with the current results.

Most previous efforts to engineer human myocardial surrogates have focused on improving the maturation status of CMs by the application of electrical or mechanical stimulation or a combination or both (with only relative success to date, see).[40,41,49–51] However, although previous studies of human-engineered cardiac constructs had found a good correlation between the degree of CM maturation achieved and the improvement in tissue-like functionality, the levels of expression of maturity-related genes indicated immature fetal-like CM properties, still far from those of adult heart. To date, the highest level of cardiac maturation achieved has been reported by the Vunjak–Novakovic´s laboratory, who demonstrated advanced features of structural and molecular maturation of human-engineered cardiac tissue after 4 weeks under electrical stimulation, but a slower and less complete functional maturation.[41] The group of W.H. Zimmermann had also previously reported the generation of engineered human myocardium with advanced maturation by applying mechanical stimulation, although they revealed enhanced expression of adult cardiac genes in the engineered tissues compared to 2D monolayers cultures, transcriptome profiling suggested that tissues are at large similar to fetal human heart at 13 weeks of gestation.[49] In our study, the MEW cardiac tissues were not subjected to electrical or mechanical stimulation and the degree of maturation achieved here is in accordance with the studies described above where electromechanical training has been used to further improve maturation, which highlights the relevance of our MEW-based system in the generation of advanced human engineered cardiac tissues. We anticipate that much longer culture times and the combination of electromechanical and metabolic stimulation would be necessary for further maturation at the CM level, and eventual cessation of spontaneous beating activity.

Taking all the above into account, we can conclude from this comparative analysis that the diamond MEW designs are able to deliver a significantly enhanced contraction, in comparison to more conventional orthogonal structures. Diamond human cardiac minitissues have larger and faster contractions, following a more aligned direction.

2.6. Diamond-MEW Minitissues have Better Calcium Conduction

In striated muscle, including the human myocardium, the arrival of the electrical wave triggers the entry of Ca from the extracellular space, as well as its massive release from the intracellular sarcoplasmic storage. The transmission of these calcium waves closely follows action potential (AP) propagation and can be used to measure conduction velocity (CV), which is enhanced upon cardiac maturation.[52] Comparative optical mapping of calcium transients (CaT) showed that CV was highest in the diamonds with 9.38 ± 1.20 cm s^{-1}. This value was significantly higher than that of the orthogonal designs (square: 6.47 ± 1.42 cm s^{-1}; rectangle 4.97 ± 1.00 cm s^{-1}, $p < 0.05$ Figure S5A, Supporting Information). Optically mapped APs and CaT of MEW minitissues showed that the AP duration (APD) and CaT duration was similar for all designs at all tested pacing frequencies (0.5–3 Hz) (Figure S5B–D, Supporting Information). In conclusion, the electrophysiological properties of the minitissues built with diamond-pore scaffolds are closer to those of human myocardium (CV: 50–100 cm s^{-1}) than for minitissues built with other scaffold-pore designs.[53–55]

2.7. Diamond-MEW Minitissues Improve Cardiac Function In Vivo

So far, our results support that the diamond MEW design seeded with hiPSC-CMs and -CFs in a fibrin hydrogel generates engineered human cardiac minitissues with advanced functionality and maturation. In order to test if the new tissues can provide therapeutic support to an infarcted myocardium, we conducted an in vivo study using a model of myocardial infarction in RNU athymic rats. This strain, which is deficient in T lymphocytes, was selected to avoid any acquired immune response to the human cells in the minitissues. Animals were subjected to permanent ligation of the left descending coronary artery and 7 days later allocated, after 3D echocardiographic confirmation of functional impairment (left ventricular ejection fraction, LVEF, <40%), to receive diamond-MEW human engineered heart tissues (MEW-hECTs), the acellular, fibrin-loaded mPCL scaffold (MEW) or equivalent suturing in the Control group. Four weeks

later, after a final 3D echocardiography, animals were humanely euthanized, and tissues fixed for subsequent analysis (**Figure 6**A). Tissues were placed following the long axis of the organ, as we reasoned this would maximize their capacity to actively provide contractile support (Figure 6B). A circumferential transplant position was ruled out due to anatomical space constrains in the animal model (difficulty to suture on the posterior surface).

Using 3D echocardiography, systolic function analysis was performed as the most accurate parameter of myocardial contractility, 4 weeks after the minitissue transplant. This analysis showed that only the myocardium treated with MEW-hECTs had a significant improvement in contractility, with a significantly higher left ventricular ejection fraction (LVEF) compared to the control group (Figure 6C). No differences in average heart rate were detected between the two groups. These data are also consistent with the fact that less ventricular dilatation was also found in the treatment group, with significantly lower end-diastolic and end-systolic volume parameters compared to the control group. These same findings of ventricular remodeling observed in the control group are consistent with the pathophysiological process that occurs in patients with chronic ischemic heart disease in routine clinical practice. In these patients, after the acute ischemic event, there is an activation of inflammatory mechanisms that produce increased fibrosis and stiffness. Changes in the collagen produced in the infarcted myocardium, cause a persistence and worsening of the absence of contractility (akinesia). This leads to a progressive deterioration of systolic function, which perpetuates and increases the thinning of the non-contractile myocardium. The result is a greater ventricular dilatation, all facilitated by a non-contractile myocardium. An ongoing remodeling process replaces dead myocardium in the ischemic area with a non-contractile scar tissue. Importantly, this was prevented in both the MEW and MEW-hECT-transplanted groups, were values for areas and volumes only increased mildly and did not change significantly. However, the contractile benefit on LVEF, was only found on the MEW-hECT group, and was accompanied by significant improvements in fractional shortening and fractional area change (FAC), which was absent for the other two control groups. All of these findings highlight once again that changes and modifications of distending or deforming forces can importantly influence ventricular enlargement and therefore the ejection fraction and ventricular function.[56] Overall, we provide for the first-time evidence of the effectiveness of MEW-based cardiac minitissues in treating a MI animal model. Although Castilho et al showed the first hiPSC-based tissues transferred to pig hearts through a minimally invasive procedure, they did not seek to assess any potential therapeutic benefit.[23] It is important to note however, that the MEW scaffold by itself was also able to contain ventricular remodeling, even if this did not translate to a benefit upon contractility (LVEF). This effect has been reported for other systems but specially for hydrogels, such as those made from decellularized ECM,[57] or hyaluronic acid,[58] the later also being explained using in silico models by decreasing fiber stress due to anisotropic stiffening.[59]

Explanted rat hearts were processed for histology after sacrifice. Sections throughout the length of the LV were stained for H&E or Sirius Red, and morphometric analysis performed. Intriguingly, this showed statistically significant differences in infarct size, measured as the area covered by the collagen scar, versus total LV area, on both Control and MEW-hECT groups versus scaffold-only transplanted animals (22.38 ± 1.06%, 14.36 ± 1.61% and 20.56 ± 1.21% for Control, MEW and MEW-hECT respectively, $p = 0.002$). Peri-infarct fibrosis, as the percentage of collagen in the infarct border, did not differ between the three groups (45.37 ± 1.21%, 47.47 ± 3.74% and 46.88 ± 1.24% for Control, MEW, and MEW-hECT respectively, $p = 0.2$) (Figure S6A,E, Supporting Information). Similarly, density of inflammatory cells in the peri-infarct zones was not different (5548 ± 116.8 cells mm^{-2}, 5275 ± 119.1 cells mm^{-2} and 5528 ± 91.78 cells mm^{-2} for Control, MEW and MEW-hECT animals respectively, $p = 0.17$, Figure S4B,E, Supporting Information). Neither vasculogenesis (density of α-SMA+ vessels) nor angiogenesis (density of small caliber BSL-I+ ones) were affected by the transplantation of the MEW minitissues (Figure S4C–E, Supporting Information). However, wall thickness was significantly increased in the MEW-hECT group, whereas a small yet non-significant increase was also produced in animals transplanted with the acellular scaffolds (Control: 901.5 ± 72.68 µm; MEW: 1087 ± 111.1 µm; MEW-hECT: 1309 ± 104.1 µm; $p = 0.036$, Figure S4E, Supporting Information), evidencing the contribution of the construct itself to this parameter.

The presence of substantial implants, evidenced by the presence of voids left by the MEW scaffold (mPCL dissolves during histological processing) and this increased in wall thickness prompted us to search for the transplanted cells. Heart sections were stained for the human marker Ku80, alongside phenotype-specific antibodies. Grafts could be identified, forming large areas in an epicardial position (Figure 6D–F). Human-iPSC-CMs $Ku80^{+}$ cells could be found in these areas in abundance, displaying well-arranged sarcomeres (Figure 6H,I). Transplanted CMs were easily distinguished, however, by their smaller size and sarcomeric content as compared with host rat CMs (also stained in green in Figure 6D,E,G). This highlights that in spite of the metabolic, gene expression, and functional maturation found in vitro, hiPSC-CMs in the minitissues are still distant from a full maturation. Here, it is plausible that extended transplantation periods can improve this.[60] No Cx43-mediated connection between the host-rat CMs and minitissue hiPSC-CMs could be found (not shown), although this cannot be excluded, given the punctuated and irregular nature of this staining in hiPSC-CMs, in contrast to the regular localization in intercalated discs in adult CMs.[61] The transplant location, mostly over the infarcted area, where few host-CMs are left after the permanent ischemia could also have a role in this. On the border zones, although rat CM-to-hiPSC-CM contacts could occur, again they were absent. Given the important electrophysiological differences between rat and human cells, with rodents having a much higher beating rate and shorter APs (reviewed in),[62] this isolation could play a positive role in protecting the graft from this mismatch, although a much detailed examination would have to be carried out to prove or disprove either possibility, especially in light of the observed improvement in contractile function.

$Ku80^{-}$ cells were also present, signaling the capacity of host cells to infiltrate the graft area. Some of these were forming vessels, that had ingrowth from the host and were connected to the endogenous circulation, as shown by the presence of erythrocytes in their lumen (Figure S7A,B, Supporting Information). The rapid appearance of vessels could be determinant for graft

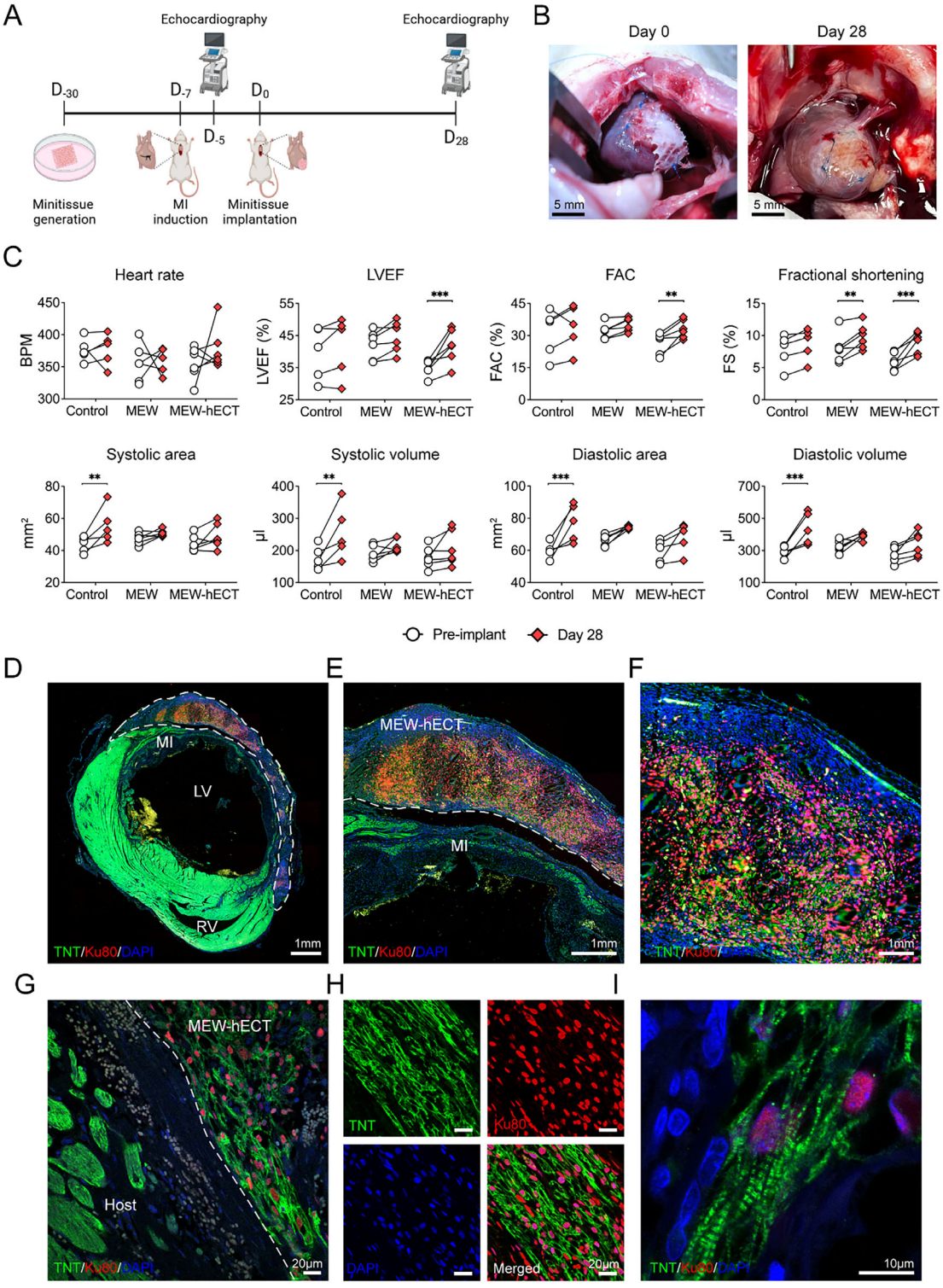

Figure 6. In vivo transplantation of diamond-pore MEW minitissues in an athymic rat model of myocardial infarction. A) Scheme of the experimental timeline (made with Biorender). B) Images of the hearts of MEW-hECT-transplanted animals on day 0 and 28, showing a good integration of the grafts, without any noticeable fibrotic encapsulation. C) 3D echocardiography analysis of cardiac function in control, MEW, and MEW-hECT groups, showing substantial benefits in minitissue-transplanted animals (MEW-hECT). D) Confocal IF localization of minitissues 28 days after transplant, showing large grafts present over the infarcted LV wall. E,F) Further magnification of the graft site, showing human $Ku80^{+}TNT^{+}$ hiPSC-CMs. G) Side-by-side comparison of the host rat CMs (green, left of dashed line) and the graft hiPSC-CMs ($Ku80^{+}$, right of dashed line). H) Detailed, single channel and composite images of grafted hiPSC-CMs. I) High magnification of engrafted hiPSC-CMs, showing the presence of prominent TNT striations. Analysis: C: two-way ANOVA followed by HSD Tukey, $*p < 0.05$; $**p < 0.01$; $***p < 0.001$.

survival, providing oxygen and nutrients to transplanted cells in the engineered tissues. Host-derived macrophages were present in the grafted areas, identified by the expression of CD68, being especially abundant in the vicinity of mPCL fibers (Figure S7C, Supporting Information), where the clustered forming giant cells. This can result from a response to the presence of the polymeric scaffold, as described for the MEW-segment of bone implants.[63] However, this did not derive in an increased density of macrophages in the infarcted or peri-infarcted areas (Figure S7D, Supporting Information). Human iPSC-CFs were also present in the grafts, identified as $Ku80^{+}VIM^{+}$ cells, interspersed with hiPSC-CMs. Some of the transplanted hiPSC-CFs expressed the myofibroblast marker α-SMA. Albeit this was not organized as filaments, ruling out a full differentiation into this pathological phenotype (Figure S7E, Supporting Information), but pointing to a proportion of cells probably initiating the process or having had initiated it in vitro, as shown by the expression of the αSMA gene, *ACTA2* (Figure S2G, Supporting Information). This can be derived from the pathological-like environment hiPSC-CFs face when transplanted, with increased levels of TGFβ, neurohormonal activation and higher mechanical stress, all known inductors of the fibroblast-to-myofibroblast transition (reviewed in).[64]

The thickness of grafts was increased in vivo to over a mm in some points (Figure 6D–F), probably through the contribution of the ingrowth host-derived cells, which includes the mentioned vessels and inflammatory cells. This has important implications as, joined with the effects on ventricular dilatation, it is plausible that the graft elicited a beneficial effect by decreasing wall stress (as per Young–Laplace's law).[65] Of note, we found that host CM size, measured as perimeter and area, was more similar to that found in healthy, non-infarcted animals, than to the control group (Figure S5E, Supporting Information). Although it could be hypothesized that the materials themselves could be source of benefit, we believe that the transient nature of fibrin precludes this effect. Also, even though this approach was tested in the past,[66] we and others have casted doubts on this mechanism.[67] The presence of large, thick grafts, alongside the absence of a significant paracrine effect (no increase in vascularization/angiogenesis or decrease in fibrosis), points to a functional contribution of the MEW minitissues to the active benefit in systolic function, as already demonstrated by Stüdemann et al.[68]

Overall, these results support the translation of the MEW cardiac tissues as a therapeutic option for MI. However, it is important to consider that the crucial role of the immune system has in the post-infarct healing phase (which covers the period when MEW tissues are transplanted here) (reviewed in ref. [69]) is partially missing in our athymic model. Although hiPSC-derived cells can potentially be applied in an autologous manner, avoiding the need of immunosuppression, it is likely that this option would impact graft survival in the long-term. Here, our minitissues were able to survive for up to 4 weeks in vivo. The presence of well-organized striations, as well as host-derived perfusion, support their capacity to survive in the longer term. In fact, the work by Kadota et al demonstrates the capacity of these cells to further mature in vivo,[60] with recent work from the same group supporting the capacity of even non-contractile hiPSC-CMs to induce a therapeutic benefit in a similar model of MI in athymic rats,[70] albeit using a higher cell dose (10^7). Hypoimmunogenic hiPSC lines have been derived and constitute an attractive option to circumvent this issue,[71] but safety concerns, especially regarding tumorogenicity, need to be examined in depth.[72] In any case, studies in large animal models such as pigs[73] or non-human primates[74] will be a must. Here, it will be important to match the design of the scaffolds to not only generate tissues that contract in-plane, but also to follow the variation in CM orientation across the epicardial surface.[75] This can be considered as negligible for the rat model, where constructs in the cm size-range are applied, but more significant for large animals (as well as human patients), where tissues will be expected to span several cms. MEW has already demonstrated the high precision and adaptability needed to fulfil this requirement.[76]

2.8. In Silico Modelling of Arrhythmogenic Potential

Further translation of MEW-based tissues into the clinical area will require safety clearance in large animal models such as pigs. For over 20 years, arrhythmogenicity has been one of the major concerns,[77] also raised more recently in non-human primate studies.[78,79] Thus, we conducted an in silico modeling and simulation study to assess the impact of the scaffold pore design on ventricular electrophysiology and proarrhythmicity, both before and after engrafting the minitissues on simulated human and porcine myocardium. We modelled minitissues built using square- and diamond-pore scaffolds (**Figure** 7A–C). The alignment of hiPSC-CMs in relation to the scaffold walls, the degree of cell-to-cell coupling, the tissue mesh properties and the cellular AP response were mathematically defined based on experimental evidence (see Experimental Section). We measured activation time (AT), conduction velocity (CV) and repolarization time gradient (RTG), the latter being characteristic of repolarization dispersion and proarrhythmic risk, in both individual and engrafted in silico minitissues, as shown in Figure 7.

We observed that the maximum AT and the mean CV were lower and higher, respectively, for diamond-pore than for square-pore minitissues, both when analyzed individually and after engrafting them on simulated human or porcine myocardium (Figure 7D,E). In the individual minitissues, the maximum AT was reduced by 8.5 ms and the mean CV was minimally incremented by 0.6 cm s^{-1} for the diamond-pore as compared to the square-pore design. When engrafted on porcine and human tissues, the maximum AT was reduced by 3.9 ms and the mean CV was increased by 0.9–1 cm s^{-1}. These results suggest that minitissues made of diamonds better replicate the anisotropy of the myocardium and result in more biomimetic activation properties, which could contribute to diminish arrhythmia vulnerability upon engraftment. Nevertheless, the mean CV in the diamond minitissues (≈12 cm s^{-1}) was still remarkably lower than the mean CV in the native myocardium (50–70 cm s^{-1}) and this may lead to ventricular re-entries after engraftment (Figure 7C), in line with the observations by Fassina et al. for slow-conducting minitissues coupled to infarcted ventricles.[80]

The mean RTG for the diamond-pore minitissues engrafted on ventricular myocardium was lower than for the square-pore minitissues, although differences were small (1.2 and 1.5 ms mm^{-1} for engraftment on porcine and human

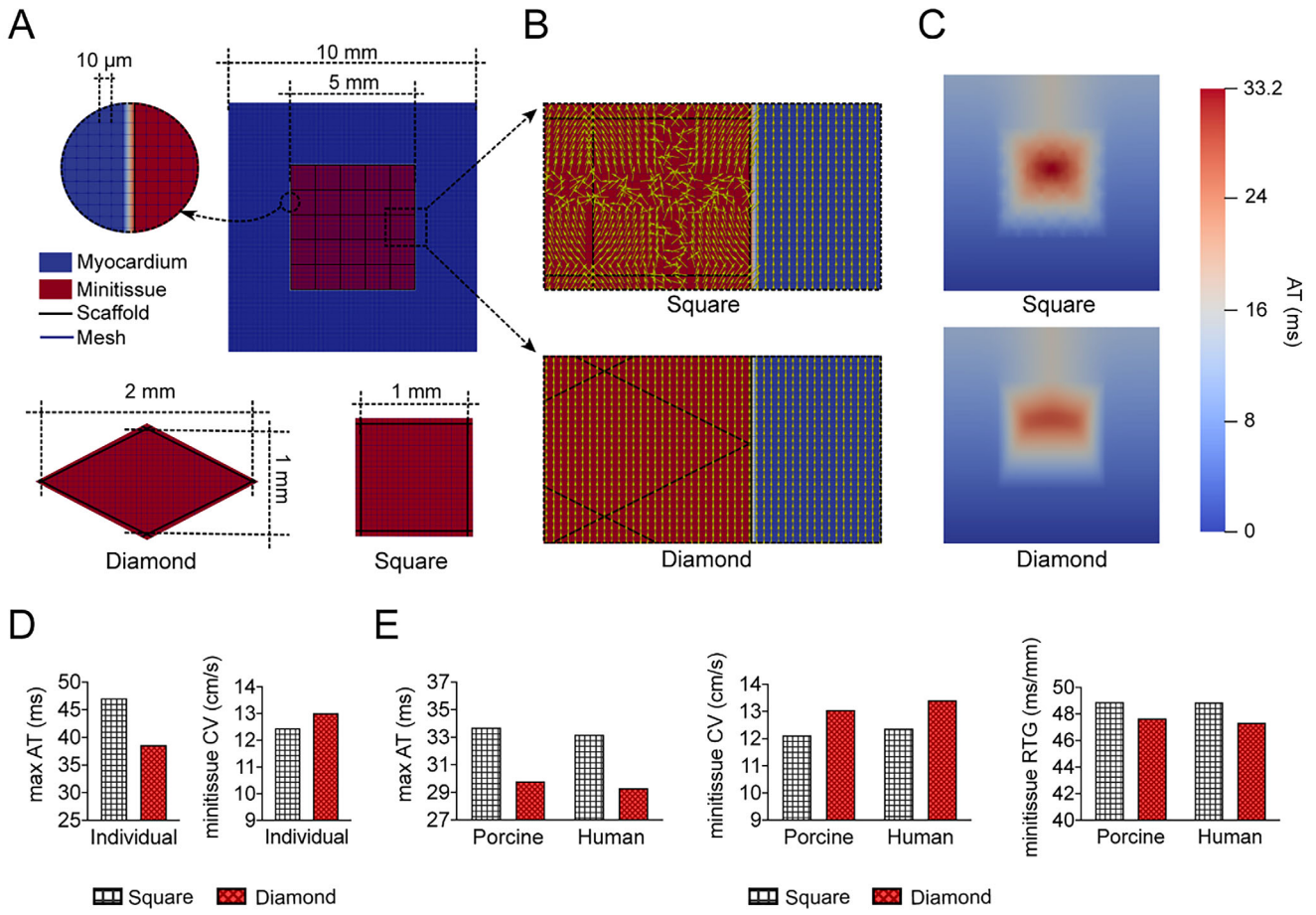

Figure 7. In silico modeling of arrhythmogenic potential of diamond-pore MEW minitissues. A) Scheme of the modeling of cardiac minitissues and its engraftment on ventricular myocardium. B) Alignment of hiPSC-CMs (yellow arrows) for square- and diamond-pore minitissues and cell alignment in the healthy myocardium. C) AT maps for square- and diamond-pore minitissues engrafted on human myocardium. D) Maximum AT and mean CV for individual square- and diamond-pore minitissues. E) Mean CV and RTG in minitissues and maximum AT for coupled minitissue-myocardium.

myocardium, respectively). The absolute mean RTG values were minimally higher for porcine than human myocardium (48.2 and 48.0 ms mm^{-1}, respectively). The moderate reduction in RTG for different alignments of hiPSC-CMs as a function of the scaffold geometry agrees with previous works[81,82] that have shown arrhythmic risk to be slightly dependent on cell orientation and to be largely determined by the degree of cell-to-cell coupling associated with the cell maturation level.[81–83] Here, we observed that diamond-pore minitissues presented enhanced maturation with respect to square-pore minitissues. Further cell-to-cell conductivity increase, associated with augmented hiPSC-CMs maturation, in diamond-pore scaffolds could help to reduce arrhythmic risk to a larger extent. Achieving this has been shown by the application of a range of interventions, from specific media to prolonged culture (reviewed in),[84] which could be applied to MEW-based engineered cardiac tissues. For example, Ronaldson-Bouchard et al. demonstrated that a progressively ramped up electrical pacing for 3 weeks resulted in one of the most advanced maturations to date, at the gene expression, ultrastructural, and functional levels.[85] From the fabrication standpoint, the present scaffold can be improved in several ways. First, although PCL is the gold standard in MEW due to its suitable properties (specially its low melting point and adequate viscosity), using a material delivering less stiff fibers would be beneficial. This could also be achieved by decreasing the PCL fiber diameter, but reproducibility of fabrication can be compromised, or stacking fewer layers. Second, if the engineered tissue is found to be pro-arrhythmogenic, a space devoid of cells can be designed, between the recipient heart and the transplanted tissue, using for example an insulating hydrogel. Finally, the translation of the contraction from the engineered tissue to the heart can be improved by adding an area with stiff fibers for an efficient force transmission. Also, matching the contraction direction to the recipient´s, as mentioned, would increase this efficiency.[75]

All in all, we found that the proarrhythmicity resulting from engrafting the engineered minitissues to native ventricular myocardium was mitigated when the minitissues were designed using diamond-pore scaffolds with respect to other geometries like square-pore scaffolds. This can be explained by the reduction in AT and increase in CV due to a better replication of myocardium anisotropy and by the reduction in repolarization heterogeneities measured by RTG.

3. Conclusion and Outlook

In this work, we show for the first time how, by using a novel diamond-pore MEW design and hiPSC-derived cells, human cardiac-engineered tissues imitating the in-plane contraction of myocardial layers can be biofabricated. These tissues display features of enhanced maturation at the metabolic and bulk gene-expression level, as compared to conventional 2D culture. Our work provides the first evidence of the capacity of MEW-based engineered cardiac tissues to support cardiac function in an animal model of myocardial infarction. Animals treated with the MEW constructs show better contractility and diminished ventricular dilatation. This correlates with the presence of large grafts containing transplanted human cells, contributing to the thickening of the ischemic myocardial wall. Finally, we use computational models of natural and engineered myocardium to show that our MEW diamond designs present decreased arrhythmogenicity, compared to conventional orthogonal structures. Overall, our work contributes to position MEW-based engineered tissues as a feasible cardiac regenerative therapy, with an optimal safety profile.

The path toward translation is now open. Although, several limitations hinder the next steps, these are already being challenged by the scientific community worldwide. A deeper knowledge on the organization, structure, and mechanics of human myocardium is required. Despite the information on porcine tissue as the closest anatomical equivalent is increasing,[24] building a highly mimetic 3D-engineered myocardium needs human-specific data. For this, advanced technologies are being applied, such as untangling the myofiber organization at high resolution with magnetic resonance diffusion tensor imaging,[86] mechanical analysis of fresh cadaveric human samples.[87] These are coupled with advanced computational models and design tools enabling the rapid printing of MEW scaffolds tailored to the specific features of each individual MI. Here, sufficient representation of specimens from both sexes will be crucial to ensure an optimal applicability and avoid later issues as for other cardiovascular applications.[88] On the biological side of the engineered tissue, the thickness of our present constructs will have to be increased to achieve a significant therapeutic effect in larger animal models and humans. The first obvious need will be the incorporation of vascularization, as ingrowth of host-derived vessels will be slower in larger mammalians than in rats, thus compromising long-term construct viability. MEW has provided excellent examples for building mm- and µm-size vessels,[89,90] also in convergence with other technologies such as volumetric bioprinting.[91] Finally, although the technical side of upscaled hiPSC-derived cardiac cell production is being tackled by using bioreactor technology and expansion protocols,[92,93] whose implementation will contribute to mitigate costs, these remain high (estimated at $800 000 for similar autologous applications).[94] In spite of the above, all the outlined advances provide reasons for optimism.

4. Experimental Section

Porcine Myocardial Fiber Orientation Assessment: Porcine hearts were obtained from a local butcher and transported to the laboratory in PBS on ice. Myocardium strips (20 × 10 × 3 mm) were dissected from the region that normally was affected after infarction. Tissue was excised, fixed in 4% paraformaldehyde, dehydrated in ethanol (4 °C, o/n) and embedded in paraffin. Tissue sections of the myocardium were cut to 4 µm thick every 0.5 mm of depth, all across the myocardial wall. The sections were deparaffinized and hydrated using serially diluted concentrations of ethanol (100%, 90%, 80%, 75%). Sections were then stained with hematoxylin-eosin, imaged, and analyzed with Orientation J, a plugin of ImageJ free software (National Institutes of Health, USA), designed to characterize the orientation and isotropy properties of an image. With this program, the frequency distribution of muscle fiber orientation was obtained for each tissue section.

Melt Electrowriting (MEW): Fibrous scaffolds were printed in mPCL (Purasorb PC12, Corbion) using a purpose-built MEW device (QUT, Queensland, Australia), as previously described.[22] Briefly, mPCL pellets were melted on a plastic syringe, to which two bars of N_2 pressure were delivered to induce material accumulation on the tip of the syringe (23 G). Voltage was gradually increased until polymer deposition started, and subsequently adjusted, in combination with the collector speed, until the jet was stable, and printing maintained (no coiling or whipping) (8.9 ± 0.3 kV and 660 ± 60 mm s^{-1}). The collector distance was kept at 8 mm. G codes with different pore geometries (squared, rectangular, and diamond-shaped) were implemented. Pore dimensions were adjusted to keep the pore area constant at ≈1 mm^2 in all cases (1000 × 1000 μm^2 for squares, 700 × 1400 μm^2 for rectangles and diamonds measuring 1000 µm in the small diagonal and 2000 µm in the big diagonal). All scaffolds used were printed with a thickness of ten layers (150 µm thick).

Scanning Electron Microscopy (SEM): Prior to scanning, mPCL scaffolds were cut to a 1 cm^2 size. Samples were then attached to Aluminum stubs using Carbon tape, gold coated in an Emitech K550X sputter coater and visualized in a Hitachi S3400N scanning electron microscope.

Mechanical Analysis of MEW Scaffolds: Uniaxial and equibiaxial tensile tests were conducted on three types of MEW-printed PCL scaffolds featuring different pore geometries: squared (SQ), rectangular (RECT), and diamond (DIAM) pores. To ensure inter-geometrical equivalence, an internal area of 1 mm^2 was maintained. The uniaxial tests were performed using a universal testing machine (Instron Microtester 5548 system) equipped with a 10 N load cell. Tests were conducted at transversal orientations relative to the pore geometry to evaluate uniaxial anisotropy, utilizing rectangular scaffold strips (40 × 10 mm). An optical measurement system (Instron 2663-281 video-extensometer) was utilized to monitor strain. Equibiaxial tests were carried out on an Instron BioPulse low-force planar biaxial testing system, accompanied by a camera system for strain tracking. Square specimens (20 × 20 mm) were prepared for equibiaxial tests. Both uniaxial and equibiaxial tests were performed under quasistatic conditions (1 mm min^{-1}) until scaffold rupture, maintaining room temperature. A minimum of eight samples for each pore geometry and testing condition were employed. Isotropy was computed as the ratio between the engineering stress on the x- and y-directions of the printing plane at 15% strain, with an isotropy ratio (IR) of 1 indicating full isotropy. The x-axis was defined as the longest direction of the pore shapes in all tests, with the y-direction being transversal to the x-axis (see Figure 4A).

hiPSC Culture and Differentiation: All experiments were performed using the WTC11 hiPSC line (UCSFi001-A, kindly donated by Prof. Bruce Conklin, Gladstone Institutes). Cells were maintained in E8 medium on growth factor reduced matrigel (GFR-MG) coated plastic surfaces (1:180 dilution), and passaged 1:15 by incubation with 0.5 mM EDTA (Invitrogen) every 4–5 days. Differentiation toward the cardiac lineage was induced using a biphasic modulation of the Wnt pathway following the protocol described by the Burridge lab.[32] Briefly, when hiPSCs achieved confluence, media were changed to RPMI supplemented with B27 minus insulin (RPMI B27−) and 8 µM GSK3 inhibitor CHIR99021 (CHIR, Axon Medchem) for 24 h. After 24 h, medium was changed to RPMI B27− for another 2 days, and then replaced with RPMI B27− and 5 µM Wnt inhibitor C59 (Axon Medchem) for 48 h. After 2 days in RPMI B27−, differentiations were maintained in RPMI supplemented with full B27 (RPMI B27). On day 9–10, contracting CMs were obtained. At this point, cells were subjected to two rounds of CM purification by culturing them for 72 h in RPMI no glucose supplemented with 4 mM lactate. Between the two cycles in lactate, the cells were replated, after incubation with TrypLE (Gibco) for 7–10

min at 37 °C. Cells were gently recovered and reseeded onto well plates coated with GFR-MG diluted 1:80 in RMPI B27. The media was supplemented with 10% Knock-out serum replacement (KSR, Gibco), and 10 μM of Y-27632 (Y27, Tocris) to enhance survival after dissociation. After 24 h, the media was changed into RPMI B27 without Y27. Cells were maintained in RPMI B27 with frequent media changes until their use, making a total of 22–25 days for the whole process.

To obtain CFs, the method described by Zhang et al.[33] was used, where Wnt pathway was first activated and cells directed toward epicardial lineage and cardiac fibroblast specification. Briefly, starting from hiPSCs at 90% confluency, cells were incubated with 5 μM CHIR on RPMI B27− for 48 h. After 24 h on RPMI B27−, cells were incubated with 5 μM C59 for 48 h. At day 5, cells were reseeded on 12 well-plated coated with Matrigel 1:80 using Advanced Dulbecco´s Modified Eagle´s Medium (ADMEM, Gibco) supplemented with 5 μM CHIR, 2 μM retinoic acid (Sigma Aldrich), 10% KSR and 10 μM Y27. The following day, the media was changed to remove Y27 and the KSR concentration was decreased to 2%. On day 8, CHIR was removed from the media and cultures were kept in ADMEM supplemented with 2% KSR kept for 72 h. At day 11, cells were dissociated and replated on 0.1% gelatin (Merck Milipore) coated 12 well plates, using Fibroblast Growth Medium 3 (FGM3, PromoCell) supplemented with 10 μM SB431542 (Sigma Aldrich), 10 ng mL^{-1} of FGF2, and 10 μM Y27. After 24 h, Y27 was removed from cell culture media and cells were maintained in culture with media changes every 2 days. On day 18, cultures of differentiated hiPSC-CFs kept with FGM3 medium supplemented with 10 μM SB431542 and 1% P/S until their use.

Flow Cytometry: Fluorescence-activated cell sorting (FACS) was performed to determine differentiation purity. For this, the Fix & Perm Kit (Invitrogen) was employed following manufacturer´s instructions, with primary antibodies against cardiac troponin T (cTNT) (1:100, Invitrogen, MA5-12960); DDR2 (1:100, Sigma Aldrich, SAB5300116); and TCF21 (1:100, Sigma Aldrich, HPA013189). Mouse IgG Alexa Fluor 488 and rabbit IgG Alexa Fluor 594 conjugated secondary antibodies (1:100, Invitrogen) were used as isotype controls. Cells were analyzed in a CytoFlex cytometer (Beckman Coulter) and data acquisition and analysis performed by FlowJo.

Cell Isolation, Tissue Generation, and Culture: Prior to cell seeding, mPCL scaffolds were cut to a 25 or 50 mm^2 size and treated with O_2 plasma (Diener Electronic) for 5 min, in order to increase their hydrophilicity and facilitate infiltration of the cell suspension. The scaffolds were then incubated in ethanol 70% during 30 min, washed thrice in sterile distilled water and left to dry. Once cell differentiation was finished, hiPSC-CMs were washed twice in 0.5 mM EDTA in PBS and incubated for 7–10 min in TryplE at 37 °C for monolayer dissociation. Cells were gently recovered, pooled, and counted. Human iPSC-CFs underwent a similar process and were added to the cell suspension in a 9:1 hiPSC-CMs: hiPSC-CFs ratio. Cell´s concentration was adjusted to 5×10^4 cells per mm^2 of scaffold. The tissue mastermix was made of cells mixed with RPMI B27 media supplemented with 10% KSR, 1% P/S, 10 μM of Y27, and 6 mg mL^{-1} bovine fibrinogen (Sigma Aldrich). For 8 mm diameter samples, 35 μL of mastermix and 1.8 μL thrombin (100 U mL^{-1} (Biopur)) were pipetted into a Teflon mold, by first dispensing half of the volume (17.5 μL of mastermix), then adding the MEW scaffold and finally the other half volume plus 1.8 μL of thrombin, followed by incubation for 1 h at 37 °C to induce fibrin crosslinking. Afterward, samples were transferred to culture plates with RPMI B27 supplemented with 10% KSR, 1% P/S, and 10 μm of Y27. On the next day, media was refreshed with RPMI B27 without Y27 and supplemented with aprotinin (0.1% (wt vol^{-1}); 33 μg mL^{-1}) (Sigma Aldrich) to avoid fibrin degradation. The medium was changed every other day.

Sample Contraction Analysis and Quantification: To investigate the effect of pore geometry on CM contraction, scaffolds of 10 × 5 mm with different pore geometries (squared, rectangular, and diamond-shaped) but comparable pore area were manufactured into several strips attached to one end (see Figure 5A). At day 27, spontaneous beating of the constructs was recorded for at least 10 s. A custom-made point tracking algorithm in MATLAB was used to obtain contraction velocity, contraction maximum displacement, and contraction trajectory.

Live/Dead Staining: Cell survival was assessed at days 1 and 14 using the Live/Dead Viability/Citotoxicity kit (Invitrogen) following manufacturer's instructions. In brief, calcein AM and ethidium homodimer were both diluted 1/500 in RPMI B27, added to samples and incubated for 45 min at 37 °C, after which media were changed and samples imaged in a Leica DMIL LED epifluorescence microscope.

AlamarBlue Assay: Cell metabolic activity was assessed using an AlamarBlue assay for cell viability (Invitrogen), following manufacturer's instructions. In brief, AlamarBlue solution was added to phenol red-free RPMI media (Life Technologies) to a final concentration of 10% (v/v), and constructs were incubated in this solution for 4 h at 37 °C. 100 μL of the supernatant was then collected in 96 well plates and measured in a plate reader (BMG Labtech).

Picogreen Assay: Cell retention within the scaffold, measured indirectly through the amount of double-stranded DNA, was examined with a PicoGreen assay (Quant-iT PicoGreen dsDNA Kit, Invitrogen), according to the manufacturer's instructions. Samples were frozen and digested overnight (o/n) at 65 °C in a 125 μg mL^{-1} papain solution (Whorthington Biochemical). DNA-induced fluorescence was measured in a fluorometer and relative cellular DNA was calculated.

RNA Extraction, RT, qPCR: Total RNA was isolated from differentiated cells and cardiac tissues using Trizol RNA Isolation Reagent (Life Technologies), following the manufacturer's instructions and 1 μg RNA was next retrotranscribed into cDNA using the Prime Script RT Reagent Kit (Takara). Quantitative real-time PCR was performed with 5 ng of cDNA in a PowerUp™ SYBR™ Green Master Mix (Applied Biosystems) and carried out in a QuantStudio 5 Fast Real-Time PCR system (Applied Biosystems). Human GAPDH was used as housekeeping gene and results were analyzed using the $2^{-\Delta\Delta Ct}$ method.

Immunostaining Analysis: For staining, engineered cardiac tissues were fixed with Zinc buffered formalin (Thermo Scientific) for 30 min at RT, followed by three washes in PBS and stored at 4 °C until use. Samples were incubated in blocking solution (PBS and 3% BSA (Sigma Aldrich)) for 20 min at RT after 0.2% Triton-X100 (Sigma Aldrich) permeabilization. Samples were stained o/n at 4 °C with anti-cardiac α-actinin (1:400, Sigma Aldrich, A7811) and anti-vimentin (1:500, Abcam, ab92547) primary antibodies diluted in 1% BSA (Sigma Aldrich). After 3 washes in PBS, samples were incubated with Alexa Fluor 488- and 594-conjugated secondary antibodies (1:500, Invitrogen) diluted in 1% BSA for 1 h at RT. Finally, samples were washed thrice with PBS and incubated with DAPI (1:500, Sigma Aldrich, D9542) diluted in PBS for 30 min at RT. Differentiated CMs and CFs seeded on Matrigel- and gelatin-coated coverslips (Ibidi) respectively, were fixed with zinc-buffered formalin for 15 min at RT. CMs were stained with primary antibodies against cardiac α-actinin and cTNT (1:200, Abcam, ab45932), and CFs with DDR2 (1:500, Sigma Aldrich, SAB5300116), and collagen I (1:100, Abcam, ab34710) antibodies. Appropriate secondary antibodies were employed (Alexa Fluor 488- or 594-conjugated, 1:500). Images were recorded using an LSM 800 Zeiss Confocal microscope, and processed using ImageJ software.

Quantification of Cell Abundance, Z-Band Spacing, and Filament Alignment: Vimentin and α-actinin confocal stacks from 3D samples were used for quantifying cell abundance, sarcomere length, and orientation. Custom macros were developed based on ImageJ (available upon request). To quantify cell abundance, between 100 and 300 hiPSC-derived cells were analyzed per plane by measuring the percentage of VIM^+ hiPSC-CF and α-$actinin^+$ hiPSC-CMs within the diamond-shaped pore. To quantify Z-band spacing and filament alignment a minimum of 20 and maximum of 40 sarcomeres were analyzed per plane, with interplane separation of at least 10 μm. The user was blinded to the group of origin to avoid any bias in the analysis.

Bulk RNA Sequencing and Analysis: Roughly 150 ng of high-quality total RNA (RIN > 8) were used for transcriptomic interrogation of engineered tissues using Illumina's Stranded mRNA Prep Ligation according to the manufacturer's instructions. Briefly, oligo(dT) magnetic beads were used to capture and purify poly-adenylated mRNA molecules from total RNA. The purified mRNA was then fragmented and reverse-transcribed to cDNA using random primers. A second strand cDNA synthesis step removed the RNA template while incorporating dUTP in place of dTTP in order to preserve strand specificity. Next, double-stranded cDNA was A-tailed, then ligated to Illumina anchors bearing T-overhangs. PCR-amplification

of the library allowed the barcoding of the samples with 10-bp dual indexes and the completion of Illumina sequences for cluster generation. Libraries were quantified with Qubit dsDNA HS Assay Kit (Thermo Fisher, Oregon, USA) and their profile was examined using Agilent's HS D1000 ScreenTape Assay (Agilent, CA, US). Sequencing was carried out in an Illumina NextSeq2000 using paired-end, dual-index sequencing (Read1: 59 cycles; i7: 10 cycles; i5: 10 cycles Rd2:59 cycles) at a depth of 30 million reads per sample. Samples were demultiplexed using Illumina *bcl2fastq* software (v.2.2.0) and aligned to the human genome (GRCh38) with STAR (V2.7.0d) using default parameters. Gene expression quantification was performed using the *featureCounts* function implemented in the R package *Rsubread* (v2.4.3) counting uniquely mapped reads with reverse strandness. The Ensembl v103 gene annotation was considered as the reference. The *filterbyExpr* function implemented in the *edgeR* package (v3.40.2) was used to filter out genes with low number of counts for downstream analyses. Data normalization, transformation (considering variance stabilizing transformation), principal component analysis and differential expression analyses were performed with the DESeq2 package (v1.30.1). To compare 3D and 2D samples at day 30, the Wald test was considered, keeping genes with an FDR of 0.05. Overrepresentation analyses of the differentially expressed genes (shrunken log2 fold-change with the lfcShrink function > 1) were performed with *enrichR* (v3.0) against the "GO_Biological_Process_2021", "BioPlanet_2019" and "MSigDB_Hallmark_2020" databases. In addition, to evaluate significant expression changes across all levels (including day 0), the Likelihood Ratio Test (LRT) with ≈1 as reduced model was considered in DESeq2. Then, the function degPatterns from the library DEGreport (v1.26.0) was used in regularized log-transformed data, obtained with the rlog function, to look for different expression patterns in those genes with an FDR < 0.05.

Optical Mapping: High temporal and spatial resolution videos of transmembrane voltage and CaT activity in the engineered cardiac tissues were recorded by optical mapping with a MiCAM O5-Ultima CMOS camera (SciMedia, Costa Mesa, CA). Tissues were stained by immersion in culture medium supplemented with RH237 (voltage-sensitive day, Invitrogen, Carlsbad, CA) at 7.5 µM for 15 min and with Rhod-2 AM (calcium-sensitive dye, Invitrogen, Eugene, OR) at 5 µM for 30 min under incubation conditions (37 °C, 5% CO_2). Blebbistatin (10 µM, Tocris Bioscience, St. Louis, MO) incubation during 30 min prevented motion artefacts. Following the incubation with the dyes, the tissues were placed in a heated chamber (RC-27NE in a PM-6 heated platform, Warner Instruments) at 36.5 °C with 1 mL pre-oxygenated Tyrode's solution (supplemented with 30 mM BDM to prevent motion artefacts). Both voltage and calcium activities were mapped using a sampling frequency of 500 Hz and a spatial resolution of 100 × 100 pixels per frame, with a field of view of 3.1 mm. The tissues were field-stimulated with two platinum electrodes using an A385 stimulator (World Precision Instruments, Sarasota, FL) to apply monopolar pulses of 70 mA amplitude and 3 ms duration. After a short period of stimulation to allow the tissues to adjust to the pacing rate, 20-s recordings were acquired at pacing frequencies of 0.5, 1, 2 and 3 Hz.

Computational Modeling and Simulation: Squared- and diamond-pore tissues were in silico modeled following the approach described in previous studies.[81] 2D meshes of 5 × 5 and 10 × 10 mm^2 were built, the former for individual tissues and the latter for tissues engrafted on healthy human or porcine myocardium. All models were discretized with 50 µm-side quadrilateral elements. In silico scaffold representations were set to replicate the experimental configurations. Square and diamond pores were generated with an area of 1 × 1 and 1 × 2 mm^2, respectively (Figure 7A). Human iPSC-CMs were oriented following experimental observations (Figure 7B). For square-pore tissues, the tissue nodes were gradually aligned following the square-pore diagonals and randomly oriented in a 0.2 mm-thick central cross. For diamond-pore tissues, as hiPSC-CMs were experimentally observed to preferentially align in the diamond's short axis, cell orientation was set parallel to this direction. The hiPSC-CMs electrical activity was described by the Paci et al. ventricular model.[95] The O'Hara-Rudy[96] and the Gaur et al.[97] models were used to represent the human epicardial and porcine ventricular APs, respectively. Electrical impulse propagation was modeled by the monodomain partial differential equation[98] and the software ELECTRA[99] as employed to numerically integrate the reaction-diffusion equation of this model. The electrical conductivity was considered to be orthotropic with transverse isotropy. A longitudinal-to-transverse ratio of 0.25 was set. Longitudinal diffusion coefficients of 0.0013 and 0.00013 $cm^2\ ms^{-1}$ were set for the ventricular myocardium and engineered tissues, respectively, to replicate experimentally reported CV ranges. Cellular models were paced to steady-state by running 2000-s simulations. The values of the model state variables at the end of pacing were used for initialization of tissue simulations, which consisted of five cardiac cycles stimulated at 1 Hz, with the last cycle being used for analysis. Stimuli of 1 ms-duration and 5 and 80 mA-magnitude were applied at the 0.5 mm inferior band of the individual and engrafted tissue meshes, respectively. A temporal resolution of 0.1 ms and a spatial resolution of 50 µm were used for numerical integration.

Surgery Animal Procedure and Study Design: All animal procedures were approved by the University of Navarra Institutional Committee on Care and Use of Laboratory Animals (CEEA) and the Navarra Regional Government (CEEA #E3-22 (043-21E1)). Ten- to 12-week-old female RH-Foxn1^{rnu} athymic nude rats (Envigo RMS Spain S.L., San Feliu de Codines, Barcelona) underwent permanent coronary artery ligation of the left anterior descending (LAD) coronary artery, as previously described.[100] Seven days post-infarction, animals underwent a second surgical procedure and two engineered cardiac tissues of 10 × 5 mm^2 size were sutured with a Prolene 7/0 non-absorbable suture (W8702, Ethicon) at four points of the heart, covering the infarcted area (MEW-hECT group). The survival rate of the course of the experiment was more than 80%. Only those animals that survived ($n = 22$) and with an ejection fraction below 40% (as determined by echocardiography at day 5 post-infarction) were included in the functional study ($n = 18$; $n \geq 5$/group). 28 days after tissue transplantation, animals were anesthetized, perfusion-fixed and killed for histological analysis. A group transplanted with only a MEW scaffold loaded with a fibrin hydrogel and cultured for 28 days (MEW group). For the Control animal group, the animals underwent the same surgical procedure without tissue implantation.

Echocardiography: Cardiac function was assessed through transthoracic echocardiography utilizing the Vevo 3100 high-resolution ultrasound system (VisualSonics, Toronto, Canada). This system was equipped with an MX550 transducer, which operated at a central frequency of 40 MHz, a focal length of 7.0 mm, and a frame rate of 557 fps in B-mode, covering a maximum field of view of 14.1 × 15.0 mm in 2D imaging. The spatial resolution was 90 µm (lateral) by 40 µm (axial), allowing high-resolution imaging. Echocardiography was performed at 5 days post-infarction and at 28 days post-transplantation. Rat anesthesia was induced by placing them in an induction chamber and administering a mixture of 4% isoflurane and 1 L min^{-1} 100% O_2. Once the animals lost their righting and digital reflex, they were carefully positioned in a supine posture on a heated pad maintained at 37 °C. The concentration of isoflurane was then adjusted to 1–2% to ensure the heart rate remained within the optimal range of 300–400 bpm during the image acquisition process. Continuous monitoring of vital parameters including heart rate, electrocardiogram (ECG), and respiratory physiology was conducted using surface ECG limb electrodes. Additionally, body temperature was meticulously monitored using a rectal probe. To optimize imaging conditions, the chests of the mice were gently shaved using a chemical depilatory cream (Veet, Reckitt Benckise, Spain), followed by the application of warmed ultrasound gel (Quick Eco-Gel, Lessa, Spain) to enhance the visibility of cardiac structures. The cardiac function of the left ventricle (LV) was evaluated using Simpson's method. This method entailed measuring end-diastolic and end-systolic areas at different LV levels (basal, middle, and apical) using the parasternal short-axis (PSAX) view in B-mode imaging. Additionally, to complete Simpson's method, the end-diastolic and end-systolic endocardial areas, along with the LV length from the aortic annulus to the apex, were measured utilizing the parasternal long-axis (PLAX) view. All images were meticulously analyzed offline using the cardiac measurement package seamlessly integrated into the VevoLab software (v5.7.1).

Tissue Processing, Staining, and Quantification: After sacrifice, hearts were excised, fixed o/n in Zinc buffered formalin at 4 °C, and cut into three equally sized blocks (apical, mid-ventricular, and basal). Next, the organs were dehydrated in 70% ethanol (4 °C, o/n), embedded in paraffin

and sectioned at a 5 µm thickness. For histological evaluation, selected sections (1 every 10 slides) were stained with hematoxylin-eosin and Sirius Red and with the appropriate antibodies. For Sirius Red staining, sections were deparaffined and immersed in 0.1% Direct Red (Sigma) in a saturated solution of picric acid for 30 min, dehydrated, and mounted in DPX (Sigma). For Hematoxylin-Eosin staining, sections were stained in Ehrlich´s hematoxylin (Sigma) for 10 min, differentiated through water-HCl and Li_2CO_3 solutions, immersed in 1% Eosin (Sigma) for 5 s, dehydrated, and mounted in DPX.

Quantification of infarct size, ventricular wall thickness, and tissue fibrosis degree was performed in stained serial sections with Sirius Red and the degree of tissue inflammation and CM hypertrophy was evaluated in hematoxylin-eosin-stained serial sections. Tissue revascularization was assessed by immunostaining techniques in the infarct border. Angiogenesis was assessed by counting the number of small vessels (capillaries) stained with lectin (1:50, BSL-I, Sigma, L3759) and using Streptavidin-Horseradish Peroxidase (HRP) conjugate (Sigma Aldrich) as secondary reagent and diaminobenzidine (Dako) as chromogen. Vasculogenesis (arterioles and arteries) was evaluated by measuring the area occupied by smooth muscle-covered vessels and by counting the number of large vessels using an anti-α-smooth muscle actin (α-SMA) primary antibody (1:200, Sigma Aldrich, A5228) and an anti-mouse IgG Alexa Fluor 488 (1:500, Invitrogen, A21202) conjugated secondary antibody.

The human cells were identified through immunofluorescence using anti-human Ku80 (1:50, Cell Signaling, 1672180S) in combination with and anti-cTNT (1:20, Abcam, ab8295) primary antibody to detect hiPSC-CMs, and with antibodies against vimentin (1:20, Abcam, ab11256) and αSMA (1:200, Sigma Aldrich, A5228) to detect hiPSC-CFs. Macrophage detection was based on the presence of CD68-positive signals (anti-CD68, 1:100, Bio-Rad, MCA341R). Appropriate secondaries antibodies were employed (conjugated to Alexa Fluor 488, Alexa Fluor 594, and Alexa Fluor 647). All primary and secondary antibodies were diluted in 1% BSA in PBS.

Bright-field digital images were acquired with an Aperio CS2 scanner (Leica Biosystems, Nussloch, Germany) and images processed with the ImageScope software (Leica Biosystems). Immunofluorescent images were acquired with a Phenoimager HT 2.0 (Akoya Biosciences) and images visualized with the Phenochart 2.0 software (Acoya Biosciences). For confocal microscopy, a LSM 800 Zeiss Confocal microscope was used. Histological and immunofluorescence preparations were quantified using ImageJ software with custom macros. Sampling and measuring were performed in all cases by an investigator blinded to the treatment of individual animals. All digital images were imported into Adobe Photoshop and formatted.

Statistical Analysis: Normal distribution of data was tested using the Shapiro–Wilk and Kolmogorov–Smirnov normality tests. All data are expressed as mean ± SEM or median (Q1, Q3) for normal and non-Gaussian distributed data. Comparisons between two groups were performed using Student's *t*-test. For experiments involving more than two groups, data were analyzed using one-way or two-way ANOVA followed by Tukey´s HSD test. Analysis were performed using GraphPad Prism 8 (GraphPad Software Inc.), and differences were considered significant when $p < 0.05$.

Supporting Information

Supporting Information is available from the Wiley Online Library or from the author.

Acknowledgements

O.I.G. and M.F.I. contributed equally to this work. This research was funded by the Ministerio de Ciencia, Innovación y Universidades CARDIOPRINT (PLEC2021-008127), VOLVAD (PID2022-142562OB-I00), and INVESTTRA (PID2022-142807OA-I00) funded by MICIU/AEI /10.13039/501100011033 and by the European Union NextGenerationEU/PRTR; the H2020 Research and Innovation Programme under grant agreements No 874827 (BRAV3); Gobierno de Navarra Proyectos Estratégicos IMPRIMED (0011-1411-2021-000096) and BIOHEART (0011-1411-2022-000071); Gobierno de Navarra Proyectos Colaborativos BIOGEN (PC020-021-022). A.U.A. was supported by a Sara Borrell grant (CD22/00027) from the Instituto Carlos III and NextGenerationEU. The authors would like to thank Dr José Valdés-Fernández for his help in formatting the manuscript.

Conflict of Interest

The authors declare no conflict of interest.

Data Availability Statement

The data that support the findings of this study are available from the corresponding author upon reasonable request. The RNA-seq data generated in this study have been deposited in the NCBI Gene Expression Omnibus (GEO) repository under accession number GSE281166.

Keywords

advanced function, aligned contraction, cardiac tissue engineering, hiPSCs, melt electrowriting, myocardial infarction, myocardial regeneration

Received: October 22, 2024
Revised: February 9, 2025
Published online:

[1] G. D. Buckberg, N. C. Nanda, C. Nguyen, M. J. Kocica, *J. Cardiovasc. Dev. Dis.* **2018**, *5*, 33.
[2] D. H. MacIver, R. S. Stephenson, B. Jensen, P. Agger, D. Sánchez-Quintana, J. C. Jarvis, J. B. Partridge, R. H. Anderson, *Eur. J. Cardiothoracic Surg.* **2018**, *53*, 112.
[3] I. J. LeGrice, Y. Takayama, J. W. Covell, *Circ. Res.* **1995**, *77*, 182.
[4] K. L. P. M. Janssens, M. Kraamer, L. Barbarotta, P. H. M. Bovendeerd, *Biomech. Model. Mechanobiol.* **2023**, *22*, 1815.
[5] S. A. Wickline, E. D. Verdonk, A. K. Wong, R. K. Shepard, J. G. Miller, *Circulation.* **1992**, *85*, 259.
[6] E. N. Farah, R. K. Hu, C. Kern, Q. Zhang, T. Lu, Q. Ma, S. Tran, B. Zhang, D. Carlin, A. Monell, A. P. Blair, Z. Wang, J. Eschbach, B. Li, E. Destici, B. Ren, S. M. Evans, S. Chen, Q. Zhu, N. C. Chi, *Nature.* **2024**, *627*, 854.
[7] K. Kanemaru, J. Cranley, D. Muraro, A. M. A. Miranda, S. Y. Ho, A. Wilbrey-Clark, K. Polanski, L. Richardson, M. Litvinukova, N. Kumasaka, Y. Qin, Z. Jablonska, C. I. Semprich, L. Mach, M. Dabrowska, N. Richoz, L. Bolt, L. Mamanova, R. Kapuge, S. N. Barnett, S. Perera, C. Talavera-López, I. Mulas, K. T. Mahbubani, L. Tuck, L. Wang, M. M. Huang, M. Prete, S. Pritchard, J. Dark, et al., *Nature.* **2023**, *619*, 801.
[8] N. S. Peters, N. J. Severs, S. M. Rothery, C. Lincoln, M. H. Yacoub, C. R. Green, *Circulation.* **1994**, *90*, 713.
[9] E. Wilkins, L. Wilson, K. Wickramasinghe, P. Bhatnagar, J. Leal, R. Luengo-Fernandez, R. Burns, M. Rayner, N. Townsend, *European Cardiovascular Disease Statistics*, European Heart Network, Brussels **2017**, 192.
[10] R. Luengo-Fernandez, M. Walli-Attaei, A. Gray, A. Torbica, A. P. Maggioni, R. Huculeci, F. Bairami, V. Aboyans, A. D. Timmis, P. Vardas, J. Leal, *Eur. Heart J.* **2023**, *44*, 4752.
[11] N. Noor, A. Shapira, R. Edri, I. Gal, L. Wertheim, T. Dvir, *Adv. Sci.* **2019**, *6*, 1900344.
[12] A. Lee, A. R. Hudson, D. J. Shiwarski, J. W. Tashman, T. J. Hinton, S. Yerneni, J. M. Bliley, P. G. Campbell, A. W. Feinberg, *Science.* **2019**, *365*, 482.

[13] M. E. Kupfer, W. H. Lin, V. Ravikumar, K. Qiu, L. Wang, L. Gao, D. B. Bhuiyan, M. Lenz, J. Ai, R. R. Mahutga, D. W. Townsend, J. Zhang, M. C. McAlpine, E. G. Tolkacheva, B. M. Ogle, *Circ. Res.* **2020**, *127*, 207.
[14] T. U. Esser, A. Anspach, K. A. Muenzebrock, D. Kah, S. Schrüfer, J. Schenk, K. G. Heinze, D. W. Schubert, B. Fabry, F. B. Engel, *Adv. Mater.* **2023**, *35*, 1.
[15] A. C. Daly, M. D. Davidson, J. A. Burdick, *Nat. Commun.* **2021**, *12*, 1.
[16] S. Choi, K. Y. Lee, S. L. Kim, L. A. MacQueen, H. Chang, J. F. Zimmerman, Q. Jin, M. M. Peters, H. A. M. Ardoña, X. Liu, A. C. Heiler, R. Gabardi, C. Richardson, W. T. Pu, A. R. Bausch, K. K. Parker, *Nat. Mater.* **2023**, *22*, 1039.
[17] J. H. Ahrens, S. G. M. Uzel, M. Skylar-Scott, M. M. Mata, A. Lu, K. T. Kroll, J. A. Lewis, *Adv. Mater.* **2022**, *34*, 1.
[18] L. A. Macqueen, S. P. Sheehy, C. O. Chantre, J. F. Zimmerman, F. S. Pasqualini, X. Liu, J. A. Goss, P. H. Campbell, G. M. Gonzalez, S. J. Park, A. K. Capulli, J. P. Ferrier, L. Mahadevan, W. T. Pu, K. K. Parker, *Biomed. Eng.* **2018**, *2*, 930.
[19] O. Bergmann, S. Zdunek, A. Felker, M. Salehpour, K. Alkass, S. Bernard, S. L. Sjostrom, M. Szewczykowska, T. Jackowska, C. Dos Remedios, T. Malm, M. Andr, R. Jashari, J. R. Nyengaard, G. Possnert, S. Jovinge, H. Druid, J. Fris, *Cell.* **2015**, *161*, 1566.
[20] K. L. O'Neill, P. D. Dalton, *Small Methods.* **2023**, *7*, 2201589.
[21] O. Bas, E. M. De-Juan-Pardo, M. P. Chhaya, F. M. Wunner, J. E. Jeon, T. J. Klein, D. W. Hutmacher, *Polym. J.* **2015**, *72*, 451.
[22] P. Montero-Calle, M. Flandes-Iparraguirre, K. Mountris, N. Laita, R. M. Rosales, O. Iglesias-García, E. M. de-Juan-Pardo, F. Atienza, M. E. Fernández-Santos, E. Peña, M. Doblaré, J. J. Gavira, F. Fernández-Avilés, F. Prósper, E. Pueyo, M. M. Mazo, *Biofabrication.* **2022**, *14*, 1504.
[23] M. Castilho, A. van Mil, M. Maher, C. H. G. Metz, G. Hochleitner, J. Groll, P. A. Doevendans, K. Ito, J. P. G. Sluijter, J. Malda, *Adv. Funct. Mater.* **2018**, *28*, 1803151.
[24] N. Laita, A. Aparici-Gil, A. Oliván-Viguera, A. Pérez-Martínez, M. Á. Martínez, M. Doblaré, E. Peña, *Acta Biomater.* **2024**, *187*, 261.
[25] B. Zhang, Y. Xiao, A. Hsieh, N. Thavandiran, M. Radisic, *Nanotechnology.* **2011**, *22*, 494003
[26] T. Arts, P. C. Veenstra, R. S. Reneman, *Am. J. Physiol.* **1982**, *243*, H379.
[27] L. Saludas, S. Pascual-Gil, F. Prósper, E. Garbayo, M. Blanco-Prieto, *J. Pharm.* **2017**, *523*, 454.
[28] J. C. Walker, J. M. Guccione, Y. Jiang, P. Zhang, A. W. Wallace, E. W. Hsu, M. B. Ratcliffe, *J. Thorac. Cardiovasc. Surg.* **2005**, *129*, 382.
[29] M. Castilho, D. Feyen, M. Flandes-Iparraguirre, G. Hochleitner, J. Groll, P. A. F. Doevendans, T. Vermonden, K. Ito, J. P. G. Sluijter, J. Malda, *Adv. Healthc. Mater.* **2017**, *6*, 1700311.
[30] G. Hochleitner, A. Youssef, A. Hrynevich, J. N. Haigh, T. Jungst, J. Groll, P. D. Dalton, *BioNanoMaterials.* **2016**, *17*, 159.
[31] T. D. Brown, P. D. Dalton, D. W. Hutmacher, *Adv. Mater.* **2011**, *23*, 5651.
[32] D. M. Lyra-Leite, H. Fonoudi, M. Gharib, P. W. Burridge, *STAR Protoc.* **2021**, *2*, 100213.
[33] H. Zhang, L. Tian, M. Shen, H. Wu, M. Gu, C. Tu, D. T. Paik, J. C. Wu, *Circ. Res.* **2019**, *125*, 552.
[34] S. Shen, L. R. Sewanan, S. Shao, S. S. Halder, P. Stankey, X. Li, S. G. Campbell, *Stem Cell Rep.* **2022**, *17*, 2037.
[35] S. Marchiano, T. Hsiang, A. Khanna, T. Higashi, L. S. Whitmore, J. Bargehr, H. Davaapil, J. Chang, E. Smith, L. P. Ong, M. Colzani, H. Reinecke, X. Yang, L. Pabon, S. Sinha, B. Najafian, N. J. Sniadecki, A. Bertero, M. Gale, C. E. Murry, *Stem Cell Rep.* **2021**, *16*, 478.
[36] Y. Y. Lam, W. Keung, C. H. Chan, L. Geng, N. Wong, D. Brenière-Letuffe, R. A. Li, Y. F. Cheung, *J. Am. Heart Assoc.* **2020**, *9*, 016528.
[37] Y. Zhao, N. Rafatian, N. T. Feric, B. J. Cox, R. Aschar-Sobbi, E. Y. Wang, P. Aggarwal, B. Zhang, G. Conant, K. Ronaldson-Bouchard, A. Pahnke, S. Protze, J. H. Lee, L. Davenport Huyer, D. Jekic, A. Wickeler, H. E. Naguib, G. M. Keller, G. Vunjak-Novakovic, U. Broeckel, P. H. Backx, M. Radisic, *Cell.* **2019**, *176*, 913.
[38] P. Carmeliet, R. K. Jain, *Nature.* **2000**, *407*, 249.
[39] G. Campostrini, L. M. Windt, B. J. Van Meer, M. Bellin, C. L. Mummery, *Circ. Res.* **2021**, *128*, 775.
[40] M. Valls-Margarit, O. Iglesias-García, C. Di Guglielmo, L. Sarlabous, K. Tadevosyan, R. Paoli, J. Comelles, D. Blanco-Almazán, S. Jiménez-Delgado, O. Castillo-Fernández, J. Samitier, R. Jané, E. Martínez, Á. Raya, *Stem Cell Rep.* **2019**, *13*, 207.
[41] K. Ronaldson-Bouchard, S. P. Ma, K. Yeager, T. Chen, L. J. Song, D. Sirabella, K. Morikawa, D. Teles, M. Yazawa, G. Vunjak-Novakovic, *Nature.* **2018**.
[42] W. Bian, C. P. Jackman, N. Bursac, *Biofabrication.* **2014**, *6*, 24109.
[43] M. L. McCain, S. P. Sheehy, A. Grosberg, J. A. Goss, K. K. Parker, *Proc. Natl. Acad. Sci.* **2013**, *110*, 9770.
[44] C. Kane, L. Couch, C. M. N. Terracciano, *Front. cell Dev. Biol.* **2015**, *3*, 59.
[45] S. D. Bird, P. A. Doevendans, A. Van Rooijen M, R. J. Hassink, R. Passier, C. L. Mummery, *Cardiovasc. Res.* **2003**, *58*, 423.
[46] J. Man, P. Barnett, V. M. Christoffels, *Cell. Mol. Life Sci.* **2018**, *75*, 1435.
[47] J. P. Goetze, B. G. Bruneau, H. R. Ramos, T. Ogawa, K. de Bold M, J. de Bold A, *Nat. Rev. Cardiol.* **2020**, *17*, 698.
[48] I. Y. Shadrin, B. W. Allen, Y. Qian, C. P. Jackman, A. L. Carlson, M. E. Juhas, N. Bursac, *Nat. Commun.* **2017**, *8*, 1825.
[49] M. Tiburcy, J. E. Hudson, P. Balfanz, S. Schlick, T. Meyer, L. M. Chang Liao, E. Levent, F. Raad, S. Zeidler, E. Wingender, J. Riegler, M. Wang, J. D. Gold, I. Kehat, E. Wettwer, U. Ravens, P. Dierickx, W. L. van Laake, M. J. Goumans, S. Khadjeh, K. Toischer, G. Hasenfuss, L. A. Couture, A. Unger, W. A. Linke, T. Araki, B. Neel, G. Keller, L. Gepstein, J. C. Wu, et al., *Circulation.* **2017**, *135*, 1832.
[50] J. Ruan, N. L. Tulloch, M. V. Razumova, M. Saiget, V. Muskheli, L. Pabon, H. Reinecke, M. Regnier, C. E. Murry, *Circulation.* **2016**, *134*, 206.
[51] S. S. Nunes, J. W. Miklas, J. Liu, R. Aschar-Sobbi, Y. Xiao, B. Zhang, J. Jiang, S. Massé, M. Gagliardi, A. Hsieh, N. Thavandiran, M. A. Laflamme, K. Nanthakumar, G. J. Gross, P. H. Backx, G. Keller, M. Radisic, *Nat. Methods.* **2013**, *10*, 781.
[52] C. Denning, V. Borgdorff, J. Crutchley, K. S. A. Firth, V. George, S. Kalra, A. Kondrashov, M. D. Hoang, D. Mosqueira, A. Patel, L. Prodanov, D. Rajamohan, W. C. Skarnes, J. G. W. Smith, L. E. Young, *Biochim. Biophys. Acta.* **2016**, *1863*, 1728.
[53] S. Shafaattalab, A. Y. Li, E. Lin, C. M. Stevens, L. J. Dewar, F. C. Lynn, S. Sanatani, Z. Laksman, R. D. Morin, F. van Petegem, L. Hove-Madsen, D. P. Tieleman, J. P. Davis, G. F. Tibbits, *Proc. Natl. Acad. Sci. USA.* **2019**, *116*, 6969.
[54] K. Lu, T. Seidel, X. Cao-Ehlker, T. Dorn, A. M. N. Batcha, C. M. Schneider, M. Semmler, T. Volk, A. Moretti, A. Dendorfer, R. Tomasi, *Theranostics.* **2021**, *11*, 6138.
[55] S. A. Watson, J. Duff, I. Bardi, M. Zabielska, S. S. Atanur, R. J. Jabbour, A. Simon, A. Tomas, R. T. Smolenski, S. E. Harding, F. Perbellini, C. M. Terracciano, *Nat. Commun.* **2019**, *10*, 2168.
[56] M. A. Pfeffer, E. Braunwald, *Circulation.* **1990**, *81*, 1161.
[57] J. D. Hunter, J. M. Mesfin, T. Ahmed, A. Chen, K. Reimold, A. Hancko, R. L. Braden, M. E. Davis, K. L. Christman, *JACC. Basic Transl. Sci.* **2024**, *9*, 322.
[58] B. P. Purcell, D. Lobb, M. B. Charati, S. M. Dorsey, R. J. Wade, K. N. Zellars, H. Doviak, S. Pettaway, C. B. Logdon, J. A. Shuman, P. D. Freels, J. H. Gorman, R. C. Gorman, F. G. Spinale, J. A. Burdick, *Nat. Mater.* **2014**, *13*, 653.

[59] E. T. Kichula, H. Wang, S. M. Dorsey, S. E. Szczesny, D. M. Elliott, J. A. Burdick, J. F. Wenk, *Ann. Biomed. Eng.* **2014**, *42*, 1546.
[60] S. Kadota, L. Pabon, H. Reinecke, C. E. Murry, *Stem Cell Rep.* **2017**, *7*, 1.
[61] A. Rodríguez-Sinovas, J. A. Sánchez, L. Valls-Lacalle, M. Consegal, I. Ferreira-González, *Int. J. Mol. Sci.* **2021**, *22*, 4413.
[62] S. Joukar, *Lab. Anim. Res.* **2021**, *37*, 25.
[63] J. A. Romero-Torrecilla, J. M. Lamo-Espinosa, P. Ripalda-Cemboráin, T. López-Martínez, G. Abizanda, L. Riera-Álvarez, R. de Galarreta-Moriones S, A. López-Barberena, N. Rodríguez-Flórez, R. Elizalde, V. Jayawarna, J. Valdés-Fernández, E. de Anleo M, P. Childs, E. de Juan-Pardo, M. Salmeron-Sanchez, F. Prósper, E. Muiños-López, F. Granero-Moltó, *NPJ Regen. Med.* **2023**, *8*, 54.
[64] N. Cadosch, C. Gil-Cruz, C. Perez-Shibayama, B. Ludewig, *Circ. Res.* **2024**, *134*, 1703.
[65] Y. C. Fung, *Biomechanics: Mechanical Properties of Living Tissues*, Springer-Verlag, New York **1981**.
[66] K. L. Christman, H. H. Fok, R. E. Sievers, Q. Fang, R. J. Lee, *Tissue Eng.* **2004**, *10*, 403.
[67] M. Araña, J. J. Gavira, E. Peña, A. González, G. Abizanda, M. Cilla, M. M. Pérez, E. Albiasu, N. Aguado, M. Casado, B. López, S. González, M. Soriano, C. Moreno, J. Merino, J. García-Verdugo, J. Díez, M. Doblaré, B. Pelacho, F. Prosper, *Biomaterials.* **2014**, *21*, 2723.
[68] T. Stüdemann, J. Rössinger, C. Manthey, B. Geertz, R. Srikantharajah, C. von Bibra, A. Shibamiya, M. Köhne, A. Wiehler, J. S. Wiegert, T. Eschenhagen, F. Weinberger, *Circulation.* **2022**, *146*, 1159.
[69] S. Steffens, M. Nahrendorf, R. Madonna, *Eur. Heart J.* **2022**, *43*, 1533.
[70] E. Karbassi, D. Yoo, A. M. Martinson, X. Yang, H. Reinecke, M. Regnier, C. E. Murry, *Circ. Res.* **2024**, *135*, 967.
[71] X. Hu, K. White, A. G. Olroyd, R. DeJesus, A. A. Dominguez, W. E. Dowdle, A. M. Friera, C. Young, F. Wells, E. Y. Chu, C. E. Ito, H. Krishnapura, S. Jain, R. Ankala, T. J. McGill, A. Lin, K. Egenberger, A. Gagnon, J. Michael Rukstalis, N. J. Hogrebe, C. Gattis, R. Basco, J. R. Millman, P. Kievit, M. M. Davis, L. L. Lanier, A. J. Connolly, T. Deuse, S. Schrepfer, *Nat. Biotechnol.* **2024**, *42*, 413.
[72] B. J. González, R. J. Creusot, M. Sykes, D. Egli, *Cell Stem Cell.* **2020**, *26*, 307.
[73] D. Selvakumar, Z. E. Clayton, A. Prowse, S. Dingwall, S. K. Kim, L. Reyes, J. George, H. Shah, S. Chen, H. H. L. Leung, R. D. Hume, L. Tjahjadi, S. Igoor, R. J. P. Skelton, A. Hing, H. Paterson, S. L. Foster, L. Pearson, E. Wilkie, A. D. Marcus, P. Jeyaprakash, Z. Wu, H. S. Chiu, C. F. J. Ongtengco, O. Mulay, J. R. McArthur, T. Barry, J. Lu, V. Tran, R. Bennett, et al., *Nat. Cardiovasc. Res.* **2024**, *3*, 145.
[74] H. Kobayashi, S. Tohyama, H. Ichimura, N. Ohashi, S. Chino, Y. Soma, H. Tani, Y. Tanaka, X. Yang, N. Shiba, S. Kadota, K. Haga, T. Moriwaki, Y. Morita-Umei, T. C. Umei, O. Sekine, Y. Kishino, H. Kanazawa, H. Kawagishi, M. Yamada, K. Narita, T. Naito, T. Seto, K. Kuwahara, Y. Shiba, K. Fukuda, *Circulation.* **2024**, *150*, 611.
[75] K. L. P. M. Janssens, P. H. M. Bovendeerd, *Biomech. Model. Mechanobiol.* **2024**, *23*, 1963.
[76] M. J. Vernon, J. Lu, B. Padman, C. Lamb, R. Kent, P. Mela, B. Doyle, A. R. Ihdayhid, S. Jansen, R. J. Dilley, E. M. De-Juan-Pardo, *Adv. Healthcare Mater.* **2022**, *11*, 2201028.
[77] P. Menasché, O. Alfieri, S. Janssens, W. McKenna, H. Reichenspurner, L. Trinquart, J. T. Vilquin, J. P. Marolleau, B. Seymour, J. Larghero, S. Lake, G. Chatellier, S. Solomon, M. Desnos, A. A. Hagège, *Circulation.* **2008**, *117*, 1189.
[78] Y. Cheng, M. L. Hsieh, C. Lin, C. M. C. Chang, C. Huang, R. Puntney, C. Ting, M. W. Nicholson, P. Lin, H. Chen, G. C. Kim, J. Zhang, J. Coonen, P. Basu, H. A. Simmons, Y. Liu, T. A. Hacker, T. J. Kamp, P. C. H. Hsieh, *Circulation.* **2023**, *148*, 1395.
[79] Y. W. Liu, B. Chen, X. Yang, J. A. Fugate, F. A. Kalucki, A. Futakuchi-Tsuchida, L. Couture, K. W. Vogel, C. A. Astley, A. Baldessari, J. Ogle, C. W. Don, Z. L. Steinberg, S. P. Seslar, S. A. Tuck, H. Tsuchida, A V. Naumova, S. K. Dupras, M. S. Lyu, J. Lee, D. W. Hailey, H. Reinecke, L. Pabon, B. H. Fryer, W. R. MacLellan, R. S. Thies, C. E. Murry, *Nat. Biotechnol.* **2018**, *36*, 597.
[80] D. Fassina, M. Bishop, G. Plank, J. Whitaker, S. E. Harding, S. A. Niederer, *Comput. Biol. Med.* **2023**, *154*, 106550.
[81] R. M. Rosales, K. A. Mountris, A. Oliván-Viguera, M. Pérez-Zabalza, G. Cedillo-Servin, O. Iglesias-García, A. Hrynevich, M. Castilho, J. Malda, F. Prósper, M. Doblaré, M. M. Mazo, E. Pueyo, *Comput. Biol. Med.* **2024**, *171*, 108044.
[82] J. K. Yu, J. A. Liang, W. H. Franceschi, Q. Huang, F. Pashakhanloo, E. Sung, P. M. Boyle, N. A. Trayanova, *Cardiovasc. Res.* **2022**, *118*, 1247.
[83] D. Fassina, C. M. Costa, S. Longobardi, E. Karabelas, G. Plank, S. E. Harding, S. A. Niederer, *PLoS Comput. Biol.* **2022**, *18*, 1010030.
[84] E. Karbassi, A. Fenix, S. Marchiano, N. Muraoka, K. Nakamura, X. Yang, C. E. Murry, *Nat. Rev. Cardiol.* **2020**, *17*, 341.
[85] K. Ronaldson-Bouchard, S. P. Ma, K. Yeager, T. Chen, L. J. Song, D. Sirabella, K. Morikawa, D. Teles, M. Yazawa, G. Vunjak-Novakovic, *Nature.* **2018**, *556*, 239.
[86] P. F. Ferreira, P. J. Kilner, L. McGill, S. Nielles-Vallespin, A. D. Scott, S. Y. Ho, K. P. McCarthy, M. M. Haba, T. F. Ismail, P. D. Gatehouse, R. de Silva, A. R. Lyon, S. K. Prasad, D. N. Firmin, D. J. Pennell, *J. Cardiovasc. Magn. Reson.* **2014**, *16*, 87.
[87] G. Sommer, A. J. Schriefl, M. Andrä, M. Sacherer, C. Viertler, H. Wolinski, G. A. Holzapfel, *Acta Biomater.* **2015**, *24*, 172.
[88] A. K. McClain, P. P. Monteleone, J. Zoldan, *Sci. Adv.* **2024**, *10*, eadn3510.
[89] M. Bartolf-Kopp, L. de Silva, A. J. W. P. Rosenberg, J. Groll, D. Gawlitta, T. Jungst, *Adv. Funct. Mater.* **2024**, *34*, 2311797.
[90] M. Ryma, H. Genç, A. Nadernezhad, I. Paulus, D. Schneidereit, O. Friedrich, K. Andelovic, S. Lyer, C. Alexiou, I. Cicha, J. Groll, *Adv. Mater.* **2022**, *34*, 2200653.
[91] G. Größbacher, M. Bartolf-Kopp, C. Gergely, P. N. Bernal, S. Florczak, M. de Ruijter, N. G. Rodriguez, J. Groll, J. Malda, T. Jungst, R. Levato, *Adv. Mater.* **2023**, *35*, 2300756.
[92] M. Prondzynski, P. Berkson, M. A. Trembley, Y. Tharani, K. Shani, R. H. Bortolin, M. E. Sweat, J. Mayourian, D. Yucel, A. M. Cordoves, B. Gabbin, C. Hou, N. J. Anyanwu, F. Nawar, J. Cotton, J. Milosh, D. Walker, Y. Zhang, F. Lu, X. Liu, K. K. Parker, V. J. Bezzerides, W. T. Pu, *Nat. Commun.* **2024**, *15*, 5929.
[93] J. W. Buikema, S. Lee, W. R. Goodyer, R. G. Maas, O. Chirikian, G. Li, Y. Miao, S. L. Paige, D. Lee, H. Wu, D. T. Paik, S. Rhee, L. Tian, F. X. Galdos, N. Puluca, B. Beyersdorf, J. Hu, A. Beck, S. Venkamatran, S. Swami, P. Wijnker, M. Schuldt, L. M. Dorsch, A. van Mil, K. Red-Horse, J. Y. Wu, C. Geisen, M. Hesse, V. Serpooshan, S. Jovinge, et al., *Cell Stem Cell.* **2020**, *27*, 50.
[94] C. A. Bravery, *Stem Cells Dev.* **2015**, *24*, 1.
[95] M. Paci, J. Hyttinen, K. Aalto-Setälä, S. Severi, *Ann. Biomed. Eng.* **2013**, *41*, 2334.
[96] T. O'Hara, L. Virág, A. Varró, Y. Rudy, *PLoS Comput. Biol.* **2011**, *7*, 1002061.
[97] N. Gaur, X. Qi, D. Benoist, O. Bernus, R. Coronel, S. Nattel, E. J. Vigmond, *PLoS Comput. Biol.* **2021**, *17*, 1009137.
[98] M. Potse, B. Dubé, J. Richer, A. Vinet, R. M. Gulrajani, *IEEE Trans. Biomed. Eng.* **2006**, *53*, 2425.
[99] K. A. Mountris, E. Pueyo, *Int. J. Numer. Method. Biomed. Eng.* **2021**, *37*, e3461.
[100] I. Perez-Estenaga, M. T. Chevalier, E. Peña, G. Abizanda, A. M. Alsharabasy, E. Larequi, M. Cilla, M. M. Perez, J. Gurtubay, F. Prosper, A. Pandit, B. Pelacho, *ACS Appl. Mater. Interfaces.* **2023**, *15*, 50638.